

Searching for Molecular Signatures in 14 Transiting Exoplanets with SPIRou

A. Masson¹, S. Vinatier², B. Bézard², F. Debras³, A. Carmona³, J. Lillo-Box¹, N. B. Cowan⁴, V. Yariv⁵, R. Allart⁶

1. Centro de Astrobiología (CAB), CSIC-INTA, Camino Bajo del Castillo s/n, 28692, Villanueva de la Cañada, Madrid, Spain

2. LIRA, Observatoire de Paris, Université PSL, CNRS, Sorbonne Université, Université Paris Cité, 5 place Jules Janssen, 92195, Meudon, France

3. Institut de Recherche en Astrophysique et Planétologie, Université de Toulouse, CNRS UMR 5277, 14 avenue Edouard Belin, 31400 Toulouse, France

4. Department of Physics and Department of Earth & Planetary Sciences, McGill University, 3550 rue University, Montréal, QC H3A 2A7, Canada

5. Institut de Planétologie et Astrophysique de Grenoble, Grenoble, CNRS, IPAG, 38000 Grenoble, France

6. Département de Physique, Institut Trottier de Recherche sur les Exoplanètes, Université de Montréal, Montréal, Québec, H3T 1J4, Canada

e-mail: amasson@cab.inta-csic.es - amasson.astro@gmail.com

Received Month dd, yyyy; accepted Month dd, yyyy

ABSTRACT

High-resolution spectroscopy provides unique constraints on exoplanet atmospheric composition and dynamics. The past decade of ground-based campaigns has accumulated extensive public archives, yet many observations remain unanalysed. We present a homogeneous blind-search analysis of 50 SPIRou transits spanning 14 exoplanets, ranging from super-Earths to ultra-hot Jupiters, combining data from large program and public archived observations. Using automated data reduction and atmospheric retrieval via Nested Sampling validated by Cross Correlation Function analysis, we confirm previous H₂O and CO detections in HD 189733 b, WASP-76 b, and WASP-127 b, report tentative H₂S detections in HD 189733 b and TOI-1807 b, tentative detection of GJ 3470 b's atmosphere, and provide upper limits for non-detections. This work demonstrates a scalable method for systematic archive analysis, providing a first step toward ground-based support of large space-based atmospheric characterization programs and the study of atmospheric diversity across exoplanet populations from a statistical perspective.

Key words. Instrumentation: spectrographs, Techniques: spectroscopic, Methods: observational, Planets and satellites: atmospheres, Planets and satellites: gaseous planets, Infrared: planetary systems

1. Introduction

Ground-based high-resolution spectroscopy (HRS, with a typical resolving power $\mathcal{R} \gtrsim 25\,000$) has emerged as a powerful method for exoplanetary atmospheric characterization. Transit observations provide access to atmospheric composition and thermal structure in planetary limbs through transmission spectroscopy (e.g., Snellen et al. 2008, 2010; Birkby et al. 2013; Brogi et al. 2018; Boucher et al. 2021). These constraints in turn provide valuable information on planetary formation pathways and migration processes in the protoplanetary disk, particularly from key elemental ratios such as O/H, C/H, and C/O (e.g., Öberg et al. 2011; Madhusudhan & Seager 2011; Moses et al. 2013; Marboeuf et al. 2014; Helling et al. 2014).

The high resolving power of ground-based spectrographs, compared with lower-resolution space-based observations, further enables Doppler-shift measurements of atmospheric dynamics and probing of higher-pressure levels less affected by cloud and haze opacity, making HRS a key complement to space-based observations (e.g., Gandhi et al. 2020). As JWST rapidly expands the sample of characterized atmospheres and Ariel is expected to eventually add hundreds more (Tinetti et al. 2018; Turini et al. 2022), ground-based HRS support is needed to provide

complementary wavelength and pressure levels coverage and enable population-level studies through homogeneous data analysis methodology.

Atmospheric characterization constitutes a primary science objective for SPIRou, a near-infrared spectropolarimeter mounted on the 3.6 m Canada-France-Hawaii Telescope (CFHT). Since its first light in 2018, three coordinated international large programs—the SPIRou Legacy Survey (SLS), SPICE (SPIRou Legacy Survey – Consolidation and Enhancement), and ATMOSPHERIX—have enabled successful H₂O and CO abundances measurements in HD 189733 b (Boucher et al. 2021; Klein et al. 2024) and WASP-76 b (Hood et al. 2024), alongside atmospheric escape detections via the metastable helium triplet (Allart et al. 2023; Masson et al. 2024). However, many targets observed within these large programs received limited per-object transit coverage due to allocation constraints, which has so far prevented robust atmospheric retrievals and left many datasets unexploited. With complementary observations now publicly available, comprehensive cross-program reanalysis becomes feasible. We present a homogeneous blind-search atmospheric analysis of 14 SPIRou transiting exoplanets spanning super-Earths to ultra-hot Jupiters, using 50 individual tran-

sits from SLS, SPICE, ATMOSPHERIX, and public archived data acquired by SPIRou. Section 2 presents the observations. Section 3 describes our data reduction and processing methodology, while Sec. 4 details the atmospheric modeling and retrieval approach. Results for each target are presented and discussed in Sec. 5, with Sec. 6 summarizing our conclusions and future prospects for HRS atmospheric characterization.

2. Observations

SPIRou’s instrumental capabilities are detailed in Donati et al. (2018, 2020); we here summarize the specifications relevant to this work. Each exposure covers a continuous spectral range between 0.95 and 2.50 μm with a resolving power of 70 000 and a sampling precision of $\sim 2.25 \text{ km s}^{-1}$ per spectral bin. The instrument operates in a cryogenic vessel at 80 K stabilized to $< 2 \text{ mK}$ precision. Data are distributed over 49 spectral orders, indexed from #31 in the red to #79 in the blue, each sampled over 4088 spectral bins. As in Masson et al. (2024), we focused our analysis on the 15 transiting short-period exoplanets observed within the SLS, SPICE, and ATMOSPHERIX large programs. Our target list hence contains 2 super-Earths (55 Cnc e, GJ 486 b), 2 sub-Neptunes (GJ 1214 b, TOI-1807 b), 5 warm Neptunes (AU Mic b, GJ 436 b, GJ 3470 b, HAT-P-11 b, K2-25 b), 2 hot Saturn (WASP-69 b, WASP-127 b), 1 warm Jupiter (WASP-80 b), 2 hot Jupiters (HD 189733 b, HD 209458 b), and 1 ultra-hot Jupiter (WASP-76 b). K2-25 b’s single transit exhibited extremely low SNR (Allart et al. 2023; Masson et al. 2024) and was discarded, reducing our sample to 14 targets. We compiled a total of 50 transits: 10 from SLS/SPICE (PI: J.-F. Donati), 16 from ATMOSPHERIX (PI: F. Debras; Debras et al. 2024; Klein et al. 2024), and 24 from public archives. The complete list of observations is detailed in Table 1. Data are available via the CADC database¹ once publicly released. Throughout this analysis, we employed the same stellar and planetary parameters as in Masson et al. (2024) and refer to their Tables 2 and 3 and references therein.

3. Data Reduction

3.1. Data preparation with APERO

Ground-based high-resolution spectroscopy of exoplanet atmospheres requires careful calibration and removal of telluric and stellar contaminants to extract the faint planetary signal. SPIRou data reduction for atmospheric characterization follows established methodologies documented in recent studies (Deibert et al. 2021; Boucher et al. 2021; Klein et al. 2024; Debras et al. 2024; Masson et al. 2024; Hood et al. 2024). We present a brief overview of our independent reduction pipeline², which applies standard HRS techniques validated through injection-recovery tests. We start with 2D (spectral order, wavelength) echelle data produced by APERO (Artigau et al. 2018), the SPIRou Data Reduction Software (DRS). These files are wavelength-calibrated (defined in vacuum through this study) and corrected for detector effects (bad pixels, instrumental background, nonlinearities, cosmic rays) and telluric transmission (Cook et al. 2022). Signal-to-noise ratios (S/N) are measured at 1.65 μm from photon counts. Since most observations were obtained in non-polarimetric mode, we used the combined flux throughout. For each transit, we used data produced with the latest DRS version

available³ for that specific observation date (Table 1). Although this required combining transits produced with different DRS versions for some targets, we found that improvements in telluric correction from newer DRS versions justified this approach.

3.2. Reduction workflow

Using the APERO produced data, our reduction workflow first correct for instrumental blaze using profiles stored in the data file. Most telluric absorption is already handled by the DRS, but some residuals remain, and the bins corresponding to the strongest corrected Earth lines exhibit large correlated noise. We therefore apply telluric lines clipping following Boucher et al. (2021) by flagging telluric lines with core transmission below 0.4 and masking spectral bins from line core up to 0.97 transmission in the wings. Each order spectrum is normalized by its median along the spectral axis, followed by an iterative $3\text{-}\sigma$ clipping using 2nd-order polynomial time-series models for each wavelength bin with a maximum of five iterations. We flatten the continuum by dividing each order by its moving average computed with a 119-pixel kernel⁴ to remove low-frequency instrumental modal noise. Data are then shifted to the stellar rest frame using $V = V_{\text{sys}} - \text{BERV}$, where V_{sys} is the systemic velocity and BERV the Barycentric Earth Radial Velocity (Wright & Eastman 2014). We remove the stellar contribution by dividing each exposure by a master spectrum built, for each transit, from an $(\text{S/N})^2$ -weighted average of both in-transit and out-of-transit observations. Including in-transit data was required to robustly estimate and correct the mean stellar spectrum. Although these data may contain planetary signal, we estimate that, for each target, the planet’s radial velocity (RV) shift during transit is large enough for this contribution to average out in the master spectrum. Our tests showed that performing this step in the stellar rest-frame resulted in a better correction of the stellar spectral signatures and extraction of the planetary signal despite the additional noise introduced when shifting and spectrally interpolating the data. Following Masson et al. (2024), a $(\text{S/N})^2$ weight was applied to any temporal combinations of the data to optimally account for the S/N temporal variations.

3.3. Additional correction with SysRem

Stellar template division removes only the temporal mean stellar signature, leaving time-variable components uncorrected. Residual variations arise from changing observing conditions, stellar activity, Rossiter-McLaughlin (RME) distortions (McLaughlin 1924), or imperfect telluric correction. We remove these percent-level residuals using the SysRem algorithm (Tamuz et al. 2005; Mazeh et al. 2007), which was reported (Birkby et al. 2013; Birkby et al. 2017; Ridden-Harper et al. 2023; Nortmann et al. 2025) to perform such correction equivalently or better than Principal Component Analysis (PCA). SysRem iteratively identifies basis vectors maximizing projected data variance while accounting for uncertainties, then subtracts projections along these principal vectors to remove correlated noise. Performing K iterations of SysRem is therefore conceptually similar to removing the K first Principal Components (PC) in a PCA-based approach,

³ We used data processed at the SPIRou Data Centre hosted at the Laboratoire d’Astrophysique de Marseille for DRS versions 0.7.294 or higher, complemented, when unavailable, with data from the CADC processed with DRS version 0.7.288.

⁴ The `convolve` method from `astropy.convolution`, which we used, requires an odd kernel.

¹ <https://www.cadc-ccda.hia-ihp.nrc-cnrc.gc.ca/>

² Available at <https://github.com/admasson/HR-SpARTA>

Table 1. Transit characteristics of the studied targets

Target	Program ID	PI	UT date [yyyy-mm-dd]	Midpoint [BJD _{TDB}]	Duration [hours]	Texp [sec]	Nexp	DRS version
55 CnC e	19AC11	E. Deibert	2019-02-14	2459213.92319	1.59	95	77	0.7.291
55 CnC e	19AC11	E. Deibert	2019-02-25	2459213.92319	1.59	95	73	0.7.291
55 CnC e	19AC11	E. Deibert	2019-04-17	2459213.92319	1.59	95	54	0.7.291
55 CnC e	19AC11	E. Deibert	2019-05-01	2459213.92319	1.59	95	73	0.7.291
55 CnC e	20BF09	F. Debras	2020-12-30	2459213.92319	1.59	45	176	0.7.291
AU Mic b	19AP42	J.-F. Donati	2019-06-17	2458651.98451	1.66	123	116	0.7.291
GJ 1214 b	19AP40	J.-F. Donati	2019-04-18	2458983.91348	0.86	602	11	0.7.294
GJ 1214 b	20AP40	J.-F. Donati	2020-05-14	2458983.91348	0.86	251	30	0.7.294
GJ 1214 b	23BF16	F. Debras	2023-09-21	2458983.91348	0.86	407	15	0.7.294
GJ 1214 b	24AF11	F. Debras	2024-03-22	2458983.91348	0.86	407	16	0.7.294
GJ 1214 b	24AF11	F. Debras	2024-04-21	2458983.91348	0.86	407	16	0.7.294
GJ 3470 b	19AP40	J.-F. Donati	2019-02-18	2458532.90622	1.39	435	32	0.7.294
GJ 3470 b	21BP40	J.-F. Donati	2021-12-15	2458532.90622	1.39	301	43	0.7.294
GJ 3470 b	22BF19	F. Debras	2023-01-06	2458532.90622	1.39	501	7	0.7.294
GJ 3470 b	23BF16	F. Debras	2023-12-29	2458532.90622	1.39	552	20	0.7.294
GJ 3470 b	24AF11	F. Debras	2024-04-04	2458532.90622	1.39	552	20	0.7.294
GJ 436 b	19AP40	J.-F. Donati	2019-02-25	2458540.10182	0.72	217	22	0.7.294
GJ 486 b	21AD97	F. Debras	2021-03-24	2459297.93910	0.97	217	30	0.7.294
GJ 486 b	21BC34	E. Deibert	2022-01-23	2459297.93910	0.97	184	42	0.7.294
GJ 486 b	22AS06	W. Wang	2022-03-11	2459297.93910	0.97	212	47	0.7.288
GJ 486 b	22AS06	W. Wang	2022-03-14	2459297.93910	0.97	212	46	0.7.288
GJ 486 b	22AS06	W. Wang	2022-04-11	2459297.93910	0.97	212	46	0.7.288
HAT-P-11 b	21AF18	F. Debras	2021-06-30	2459395.93748	2.41	323	44	0.7.294
HAT-P-11 b	21BF19	F. Debras	2021-08-18	2459395.93748	2.41	323	44	0.7.294
HAT-P-11 b	21BC09	M. Radica	2021-08-13	2459395.93748	2.41	284	46	0.7.288
HAT-P-11 b	22AF11	F. Debras	2022-06-12	2459395.93748	2.41	323	37	0.7.294
HD 189733 b	18BD50	C. team	2018-09-22	2458383.80116	1.97	251	36	0.7.294
HD 189733 b	19AP40	J.-F. Donati	2019-06-15	2458383.80116	1.97	251	50	0.7.294
HD 189733 b	20AC01	E. Deibert	2020-07-03	2458383.80116	1.97	95	54	0.7.294
HD 189733 b	20AC01	E. Deibert	2020-07-05	2458383.80116	1.97	95	52	0.7.294
HD 189733 b	20AC01	E. Deibert	2020-07-25	2458383.80116	1.97	95	124	0.7.294
HD 189733 b	21BC16	E. Deibert	2021-08-24	2458383.80116	1.97	95	108	0.7.291
HD 189733 b	23BO37	A. Oklopčič	2023-08-04	2458383.80116	1.97	95	84	0.7.291
HD 189733 b	23BO37	A. Oklopčič	2023-08-24	2458383.80116	1.97	95	80	0.7.291
HD 189733 b	24AF11	F. Debras	2024-05-25	2458383.80116	1.97	301	30	0.7.294
HD 189733 b	24AC16	R. Allart	2024-06-25	2458383.80116	1.97	95	112	0.7.290
HD 209458 b	19AF16	G. Hebrard	2019-06-18	2458653.03998	3.09	903	18	0.7.294
TOI-1807 b	21BD87	B. Klein	2022-01-12	2459684.94696	1.00	362	20	0.7.291
TOI-1807 b	22AF11	F. Debras	2022-04-15	2459684.94696	1.00	362	20	0.7.294
TOI-1807 b	22AF11	F. Debras	2022-06-09	2459684.94696	1.00	362	20	0.7.294
WASP-127 b	20AP42	J.-F. Donati	2020-03-11	2458919.96815	4.54	301	50	0.7.294
WASP-127 b	21AC02	A. Boucher	2021-03-22	2458919.96815	4.54	501	28	0.7.294
WASP-127 b	21AC02	A. Boucher	2021-05-03	2458919.96815	4.54	501	20	0.7.294
WASP-127 b	23BC26	A. Boucher	2023-12-28	2458919.96815	4.54	501	30	0.7.288
WASP-127 b	23BC26	A. Boucher	2024-01-22	2458919.96815	4.54	501	30	0.7.288
WASP-69 b	19BP40	J.-F. Donati	2019-10-13	2458769.85111	2.23	123	93	0.7.294
WASP-76 b	20BF09	F. Debras	2020-10-31	2459153.88490	3.75	774	27	0.7.288
WASP-76 b	21BF19	F. Debras	2021-10-28	2459153.88490	3.75	774	26	0.7.294
WASP-76 b	21BS19	G. Chen	2021-09-18	2459153.88490	3.75	301	61	0.7.288
WASP-80 b	19BP40	J.-F. Donati	2019-10-07	2458763.77156	1.27	184	74	0.7.291

Notes. Transit midpoints were computed using the periods and midpoint reference values from the ExoClock* database (Kokori et al. 2022a,b, 2023). All dates are defined in Barycentric Julian Date (BJD) expressed in the Dynamic Barycentric Time standard (TDB), the proper time definition for defining interstellar events (Eastman et al. 2010). "Duration" is the transit duration, in hours. "Texp" is the exposure time, in seconds, of a single exposure. "Nexp" is the total number of exposures collected during the transit. "DRS version" is the version of the Data Reduction Software used to pre-process the data (see Sec. 3).

* <https://www.exoclock.space/>

with the added advantage that SysRem accounts for varying uncertainties in the data.

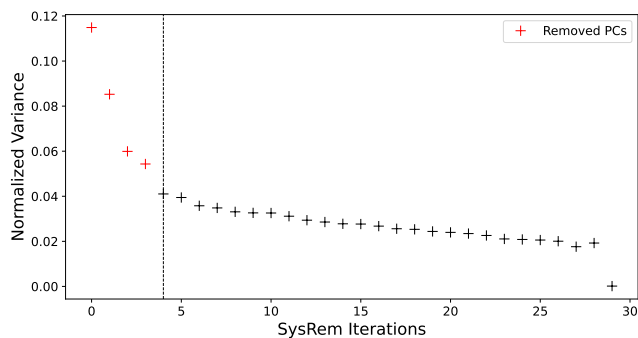


Fig. 1. Example of the data variance explained per SysRem iteration for order #68 of the WASP-127 b 2023 transit. The vertical dashed line marks the Kneedle-identified elbow giving the optimal number of SysRem iterations/PCs to remove (red crosses). The final zero-variance point—due to the dimensionality reduction caused by the mean stellar template removal—was excluded from the Kneedle analysis.

Determining the optimal number of iterations per spectral order is critical: too few iterations leave correlated residuals, while too many may suppress the planetary signal. A common approach is to tune this number by maximizing the recovered planet signal, but this method has been shown to potentially bias and artificially increase the resulting S/N (Cabot et al. 2019; Cheverall et al. 2023). The data variance explained per SysRem iteration follows a linear trend for pure Gaussian noise but exhibits an "elbow" shape in real data, where early iterations remove high-variance systematics before transitioning to a noise-dominated regime (Fig. 1). We employ the Kneedle⁵ algorithm (Satopaa et al. 2011)—designed to detect elbow positions in 1D curves—to automatically determine the optimal number of SysRem iteration per order. This approach is faster, less biased than methods maximizing output planetary signals, and allows for blind automation of residual noise removal in the observed data. We validated our approach with injection-recovery tests and found that i) SysRem slightly outperforms PCA, ii) applying the method to the data in log-flux space slightly improves performance, and iii) optimizing the per-order number of SysRem iterations with Kneedle yielded better correction. Following this noise removal step with SysRem, a final sigma-clipping stage removes any remaining outliers based on spectral variance trends (Appendix 6.1). All reduced data obtained from the above steps are publicly accessible on the associated online repository⁶.

4. Method

4.1. Modeling the transmission signature

We compute atmospheric transmission spectra using petitRADTRANS (Mollière et al. 2019, 2020; Alei et al. 2022; Blain et al. 2024; Nasedkin et al. 2024), which performs 1D radiative transfer given planetary bulk parameters, thermal profiles, and composition. The code accounts for H₂ and He Rayleigh scattering, H₂-H₂ and H₂-He collision-induced absorptions, and optically thick gray cloud decks at a given pressure level. We assume hydrogen-dominated⁷ atmospheres

⁵ <https://github.com/arvkevi/kneed>

⁶ <https://cloud.cab.inta-csic.es/s/JwKnrYqCFgAsdJb>

⁷ Although 55 Cnc e, GJ 486 b, and TOI-1807 b may not host primary atmospheres (in which case the retrieved parameters would be physi-

cally non-informative), we retain an H₂-dominated assumption for all targets to keep the blind-search analysis homogeneous.

with 75/25 H₂/He mass ratio and used a pressure grid of 130 layers logarithmically spaced from 10⁻⁸ to 10² bar. We used the line-by-line mode to compute the wavelength-dependent apparent planetary radius R_{λ} at a resolving power of 10⁶. We reduced computation time by setting petitRADTRANS' wavelength sampling parameter to 4, reducing the model's sampling while maintaining at least 2 times oversampling relative to the data. We construct time-varying transmission spectra $T_{\lambda}(t) = 1 - W(t)(R_{\lambda}/R_{\star})^2$, where R_{\star} is the host star radius, and $W(t)$ is the transit light curve computed via batman (Kreidberg 2015) taking into account orbital parameters and quadratic limb darkening. Rotational broadening due to atmospheric rotation is applied via RotBroadInt (Carvalho & Johns-Krull 2023), then spectra are convolved to instrumental resolution and shifted to the stellar rest frame using the KeplerEllipse model from pyastronomy to account for orbital geometry and eccentricity. The model is then sampled onto SPIRou wavelength bins and orders, convolved at the instrumental resolution, and broadened for each exposure to account for the smearing induced by the planet's radial-velocity shift during exposures. We must then apply the same degradation to the planetary transmission model as induced by our reduction pipeline. For the moving average division, we divide each synthetic spectral order by its smoothed version using an identical kernel size (Section 3.2). For the systematic noise removal with SysRem, we follow Gibson et al. (2022): during reduction, we precomputed and stored the $\mathbf{U}\mathbf{U}^{\dagger}$ product for each spectral order, where \mathbf{U} contains the first left singular vectors from each SysRem iteration and \mathbf{U}^{\dagger} is its Moore-Penrose inverse. We thus multiply each spectral order by the corresponding $\mathbf{U}\mathbf{U}^{\dagger}$ product to apply SysRem's signal removal effect to the model with minimal computational overhead.

4.2. Nested Sampling

We employed Nested Sampling via pymultinest (Buchner et al. 2014; Feroz & Hobson 2008; Feroz et al. 2019) for atmospheric parameter inference, chosen for its computational efficiency relative to MCMC (Klein et al. 2024). We used a Gaussian likelihood:

$$\ln \mathcal{L} = -\frac{1}{2} \sum_i \left[\frac{(d_i - m_i)^2}{\sigma_i^2} + \ln(2\pi\sigma_i^2) \right] \quad (1)$$

where d_i is the reduced data, m_i the model, σ_i the uncertainty, and i sums over wavelength and time. As in Masson et al. (2024), the uncertainty were estimated by computing the (S/N)²-weighted standard deviation of each spectral bin along the time axis. For multi-transit targets, we co-added log-likelihoods across all transits. We restricted retrievals to isothermal atmospheres with uniform abundances due to computational constraints, searching for H₂O, CO, CH₄, NH₃, CO₂, H₂S, HCN, C₂H₂, and OH (opacity sources in Table 4). We adopted a two-stage retrieval approach to handle the distinct requirements of detections versus non-detections. The *Full Run* optimized 15 free parameters (Kp, V_0 , T_{iso} , abundances in mass mixing ratio 'MMR', V_{rot} , and cloud pressure level P_{cl}) to obtain constraints on clearly identified planetary signatures. However, when no clear detection exists, high-dimensional parameter degeneracies and residual noise cause the algorithm to converge toward spurious stellar or telluric features in the (Kp, V_0) plane rather

cally non-informative), we retain an H₂-dominated assumption for all targets to keep the blind-search analysis homogeneous.

than finding realistic atmospheric constraints. We therefore performed an *Upper Limits Run* all parameters held fixed except for molecular abundances, to prevent spurious convergence. For this run, the temperature profile was set to non-isothermal using EXOREM’s `c1oud_500`⁸ theoretical grid, a 1D radiative-convective equilibrium model that simulates planetary atmospheres by accounting for cloud formation and chemical disequilibrium effects (Baudino et al. 2015, 2017; Charnay et al. 2018; Blain et al. 2021). For this run, we also fixed K_p to its planetary values, V_0 to 0 km s⁻¹, and excluded rotational broadening and clouds. Both runs used 400 live points. Constraints are then derived from the posterior distributions: for converged runs we report the median and the 16th–84th (1 σ) percentile interval, while for non-converged runs we report the 99.7th percentile as the 3- σ upper limit.

4.3. Cross Correlation Function

Nested Sampling can be sensitive to convergence on telluric or stellar residuals, so we employed the Cross Correlation Function (CCF) technique as an independent verification method. For each potential detection, and using same notation as Eq. (1), we computed $CCF = \sum_i \frac{d_i m_i}{\sigma_i^2}$ (Snellen et al. 2010), evaluated as a function of K_p and V_0 by shifting the planetary model in the stellar rest frame. We converted CCF maps to S/N maps by dividing each value by the standard deviation of the CCF in a region far from the expected planetary signature, following standard practice (e.g., Boucher et al. 2021; Klein et al. 2024; Hood et al. 2024). To properly estimate the CCF variance, we sampled 500 K_p values (0–500 km s⁻¹) and 200 V_0 values (-100–100 km s⁻¹), excluding a masked region of ± 100 km s⁻¹ in K_p and ± 25 km s⁻¹ in V_0 around the expected planetary position. Our detection criterion requires: (i) Nested Sampling convergence to a solution consistent with the planetary K_p and V_0 , and (ii) a CCF signature with SNR ≥ 5 at that location. Signatures with SNR in the [3–5] range were flagged as tentative.

5. Results

5.1. 55 Cnc e

Discovered in 2004 (McArthur et al. 2004; Dawson & Fabrycky 2010), this $\sim 1.8 R_\oplus$, $\sim 8 M_\oplus$ super-Earth (Bourrier et al. 2018) may host a hot, possibly lava-driven secondary atmosphere (Ridden-Harper et al. 2016; Demory et al. 2016; Taberner et al. 2021; Deibert et al. 2021; Mercier et al. 2022; Keles et al. 2022; Rasmussen et al. 2023; Hu et al. 2024). HCN was tentatively reported with HST/WFC3 (Tsiaras et al. 2016a), while recent JWST observations allow for a CO₂-rich atmosphere (Hu et al. 2024). We reanalyzed the four SPIRou transits from Deibert et al. (2021) plus one ATMOSPHERIX transit (Table 1). The *Full Run* converged on residuals without constraining parameters, and the *Upper Limits Run* yielded unrealistically high CO₂ abundances at the prior’s edge (Fig. 9), making this parameter uninformative. Computing the CCF map corresponding to the best retrieved abundances results in a marginal 3.2- σ peak at the expected planetary (K_p , V_0) position, driven primarily by CO₂. A similar marginal signal was noted by Deibert et al. (2021) without conclusive interpretation. Given the modest sensitivity of five SPIRou transits for detecting 55 Cnc e’s expected confined atmosphere, this signal is most likely spurious noise

⁸ <https://gitlab.obspm.fr/Exoplanet-Atmospheres-LESIA/exorem>

or telluric contamination. We hence report no atmospheric detection, consistent with prior non-detections of a primary H₂/He envelope (Ehrenreich et al. 2012; Angelo & Hu 2017; Esteves et al. 2017; Zhang et al. 2021; Deibert et al. 2021; Masson et al. 2024). Additional transits and joint analyses with other facilities will be needed to improve constraints, as well as separate retrievals with non-H₂-dominated compositions to quantify their impact on posterior constraints and Bayesian model evidence.

5.2. AU Mic b

Discovered in 2020 (Plavchan et al. 2020), this warm sub-Neptune (0.037 M_{Jup}, 0.37 R_{Jup}, Zicher et al. 2022) orbits a young (22 \pm 3 Myr, Mamajek & Bell 2014) M-dwarf. The notorious host star activity has made previous atmospheric characterization attempts extremely challenging (e.g., Palle et al. 2020b; Rockcliffe et al. 2023; Masson et al. 2024). With only a single transit available, incomplete removal of the stellar signature caused the *Full Run* to converge toward stellar residuals rather than planetary signal. Retrieving meaningful constraints for this target required stronger model assumptions through the *Upper Limits Run*, resulting in the abundance upper limits reported in Table 3. Our CCF analysis using these best-fit parameters revealed no planetary signature (Fig. 9). Accumulating additional transit observations over longer timescales may eventually enable atmospheric detection by increasing signal-to-noise ratio while averaging out stellar activity contributions.

5.3. GJ 1214 b

Discovered in 2009 (Charbonneau et al. 2009), GJ 1214 b is a sub-Neptune (0.025 M_{Jup}, 0.24 R_{Jup}; Cloutier et al. 2021) on a 1.58-day orbit around an M dwarf. Analysis of the five transits from the *Full Run* retrieval and CCF reveal strong low- K_p telluric residuals that prevent a robust atmospheric retrieval⁹. Letting only abundances free in the *Upper Limits Run*, we obtain upper limits for all species except H₂O; the latter remains biased by telluric contamination (Table 3). This non-detection aligns with previously reported flat spectra and remains compatible with a dense high-altitude cloud deck and/or high metallicity (e.g., Bean et al. 2010, 2011; Désert et al. 2011; Berta et al. 2012; de Mooij et al. 2012; Miller-Ricci Kempton et al. 2012; Teske et al. 2013; Valencia et al. 2013; Kreidberg et al. 2014; Cloutier et al. 2021).

5.4. GJ 3470 b

Discovered in 2012 (Bonfils et al. 2012), this sub-Neptune (0.04 M_{Jup}, 0.35 R_{Jup}; Kosiarek et al. 2019) orbits an M dwarf in 3.3 days and exhibits atmospheric escape (e.g., Ninan et al. 2020; Palle et al. 2020a; Lampón et al. 2023; Allart et al. 2023; Masson et al. 2024). Early observations yielded flat spectra, consistent with clouds, high metallicity, and CH₄ depletion from disequilibrium chemistry (Nascimbeni et al. 2013; Crossfield et al. 2013; Dragomir et al. 2015). H₂O was detected with HST and Spitzer (Benneke et al. 2019), later confirmed by JWST (Beatty et al. 2024) along with CH₄, CO, CO₂, and SO₂. The SO₂ detection further indicates that photochemical processes contribute to disequilibrium chemistry in GJ 3470 b’s upper atmosphere. Dash

⁹ Corner plots and CCF maps for GJ 1214 b, GJ 436 b, HAT-P-11 b, and WASP-80 b are accessible as Fig. 14 to 17 on <https://cloud.cab.inta-csic.es/s/Ss7GDRbz6MySNZ>

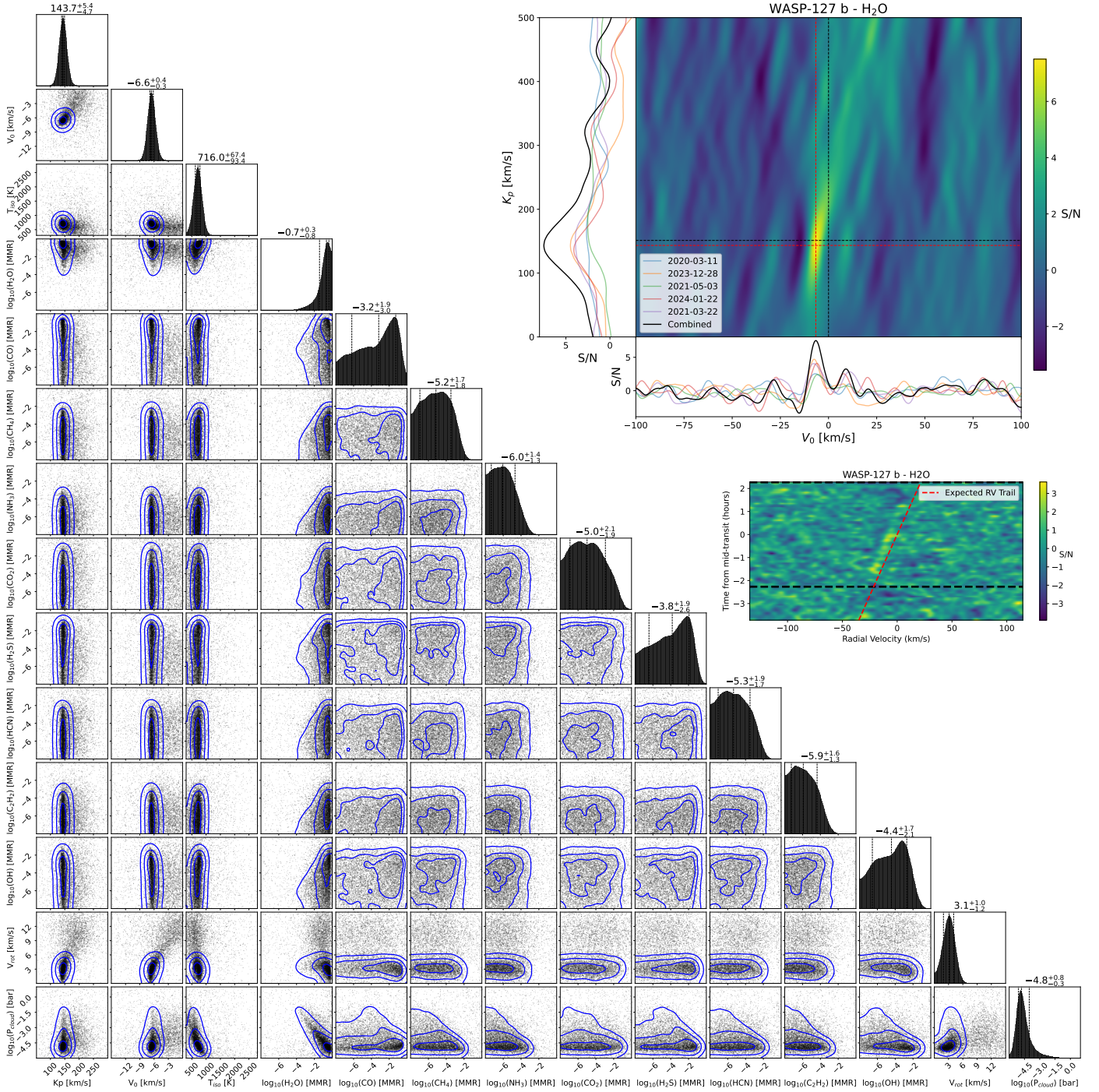


Fig. 2. Results for WASP-127 b. **Bottom Left:** Corner plot from the *Full Run* showing 1-, 2-, and 3- σ confidence contours (blue) with median posterior values and 1- σ errors above each distribution. **Upper Right:** CCF maps for different molecular species (see titles). The expected planetary position is marked with a black cross; the best-fit retrieval position (K_p , V_0) is shown as a red cross. Left and lower panels display the projected CCF at the best (K_p , V_0) for each transit (color-coded) and their combination (black). A phase-resolved CCF is also shown, displaying the planetary H_2O signature detected during transit (horizontal dashed black line) and following the expected planetary RV trail in the stellar rest frame (red dashed line).

et al. (2024) analyzed two CARMENES transits but were unable to detect H_2O .

Our *Full Run* analysis (Fig. 11) of five SPIRou transits yields puzzling constraints. The retrieved K_p (128^{+17}_{-16} km s $^{-1}$) is consistent with the planetary value, while V_0 (-5.4 ± 0.8 km s $^{-1}$) and V_{rot} ($4.0^{+1.7}_{-1.9}$ km s $^{-1}$) are plausible for atmospheric circulation. However, several parameters are physically problematic: the temperature ($T_{iso} = 1100^{+70}_{-100}$ K) is approximately twice

the equilibrium value (615 ± 16 K; Kosiarek et al. 2019) and incompatible with Beatty et al. (2024)’s thermal profile. The retrieved CH_4 abundance ($\log_{10}(CH_4) = -1.4^{+0.5}_{-0.6}$ MMR, or $-2.3^{+0.8}_{-1.0}$ VMR, Volume Mixing Ratio) contradicts JWST’s measurement ($-4.05^{+0.25}_{-0.27}$ VMR; Beatty et al. 2024). The OH abundance converges at the prior’s upper edge, despite OH requiring ultrahot Jupiter conditions for H_2O dissociation (Nugroho

et al. 2021; Choi et al. 2025; Yang et al. 2025). Furthermore, like Dash et al. (2024), we detect no H₂O, CO, or CO₂—the dominant JWST species (Beatty et al. 2024). These contradictions suggest residual stellar contamination biases the *Full Run* results. The CCF computed from these abundances shows a 4.3- σ OH-dominated peak near the expected (Kp, V₀) position. This is inconsistent with telluric contamination but could originate from M-dwarf activity or the Rossiter-McLaughlin effect. However, the signal morphology is unusual: stellar contamination typically produces symmetric ‘V-shaped’ features extending to Kp \sim 0 (see e.g. Chiavassa & Brogi 2019), absent in Figure 11. One explanation could be that our reduction—notably the SysRem correction—preferentially subtracts stationary or slowly shifting stellar components, so the low-Kp stellar signal is corrected more strongly, while high-Kp stellar residual can persist and mimic a planetary. Alternatively, the presence of OH in the upper atmosphere is required to explain the photochemically produced SO₂ detected by Beatty et al. (2024). It may therefore be possible to constrain an OH abundance profile from their SO₂ detection and estimate if the escaping planetary atmosphere could contribute to some extent to the observed CCF signal. Such analysis would require advanced photochemistry modeling coupled with atmospheric escape simulations and is therefore left for future work.

5.5. GJ 436 b

Discovered in 2004 (Butler et al. 2004), GJ 436 b is a sub-Neptune (0.45 M_{Jup}, 0.43 R_{Jup}; Maxted et al. 2022) on a 2.6-day orbit around an M dwarf. The planet hosts a large comet-like hydrogen exosphere (Kulow et al. 2014; Ehrenreich et al. 2015; Lavie et al. 2017; dos Santos et al. 2019), and Spitzer data indicate a CO-rich, CH₄-depleted, highly metallic atmosphere (Stevenson et al. 2010; Madhusudhan & Seager 2011; Line et al. 2014). Previous ground-based efforts have reported non-detections of FeH (Kesseli et al. 2020), H₂O, CH₄, or CO (Grasser et al. 2024). With only one SPIRou transit, the *Full Run* did not yield meaningful constraints. Results from the *Upper Limits Run* favor high CO₂ and HCN abundances, yet with no detection from the CCF analysis and errors too large to obtain conclusive upper limits. Our search for atmospheric signature is therefore inconclusive and will require stacking additional transits, potentially with multiple instruments, to reach constraining sensitivity.

5.6. GJ 486 b

Discovered in 2021 (Trifonov et al. 2021), GJ 486 b is a 1.3 R_⊕, 2.8 M_⊕ planet on a 1.5-day orbit around an M dwarf. Formation scenarios span from a bare rock to an H/He envelope with solar or enhanced metallicity, with an H₂O-dominated atmosphere deemed most likely (Caballero et al. 2022). JWST observations reported a flat spectrum compatible with a water-rich atmosphere or an airless body (Moran et al. 2023). Ground-based searches reported non-detections of H₂O, CH₄, NH₃, HCN, CO₂, CO (Ridden-Harper et al. 2023) and no metastable He escape (Masson et al. 2024). Our *Full Run* analysis of the five SPIRou transits shows no clear planetary signature, while the *Upper Limits Run* statistically favors CO ($\log_{10}(\text{CO}) = -2.7^{+1.1}_{-1.6}$) and H₂S ($\log_{10}(\text{H}_2\text{S}) = -3.8^{+1.1}_{-2.7}$) but without supporting CCF detections (Fig. 10). We therefore report no atmospheric detection, with upper limits indicated in Table 3.

5.7. HAT-P-11 b

Discovered in 2010 (Bakos et al. 2010), this low-mass hot-Neptune (25.7 M_⊕, 4.7 R_⊕) orbits a K star on a 4.89 days eccentric orbit ($e \sim 0.26$; Huber et al. 2017), allowing for clear stellar-planetary separation. Prior studies detected H₂O (e.g., Fraine et al. 2014; Cubillos et al. 2022) and atmospheric escape (e.g., Allart et al. 2018; Dos Santos et al. 2022; Masson et al. 2024). Chachan et al. (2019) reported tentative CH₄, while Basilicata et al. (2024) detected H₂O and NH₃, with tentative CO₂ and CH₄, but no C₂H₂, HCN, or H₂S from four GIANO-B transits. Our four-transit *Full Run* yields no meaningful constraints. The *Upper Limits Run* converges to extreme CH₄ and H₂S at prior boundaries and $\log_{10}(\text{HCN}) = -4.5^{+1.4}_{-1.9}$ MMR, all without CCF confirmation. We conclude to a non-detection of HAT-P-11 b atmosphere, and report 3- σ upper limits in Table 3.

5.8. HD 189733 b

Discovered in 2005 (Bouchy et al. 2005), HD 189733 b is a hot-Jupiter (1.16 M_{Jup}, 1.12 R_{Jup}; Alonso-Floriano et al. 2019) on a 2.2-day orbit around a K star. Its atmosphere exhibits well-established detections of H₂O, CO, and CO₂ from space and ground-based observations (e.g., Swain et al. 2009; Birkby et al. 2013; Sing et al. 2016; Brogi & Line 2019; Alonso-Floriano et al. 2019; Boucher et al. 2021; Blain et al. 2024), with recent JWST constraints on H₂O, CO₂, CO, and H₂S (Fu et al. 2024). We analyzed eight SPIRou transits, excluding two with low SNR and poor time coverage (2020-07-03, 2020-07-05; Table 1), and including the two transits studied by Boucher et al. (2021). The *Full Run* converges to Kp = 138.3 $^{+7.3}_{-7.0}$ km s⁻¹ and V₀ = -3.7 $^{+0.4}_{-0.3}$ km s⁻¹ (Fig. 7). This blueshift is consistent with prior measurements (-3.9 ± 1.3 km s⁻¹ in Alonso-Floriano et al. 2019; -4.62 $^{+0.46}_{-0.44}$ km s⁻¹ in Boucher et al. 2021) and theoretical predictions for day-night wind circulation in hot Jupiters. Rotational broadening V_{rot} = 2.3 $^{+1.1}_{-1.2}$ km s⁻¹ matches the expected equatorial velocity under tidal locking (~ 2.6 km s⁻¹). Our best-fit atmospheric model disfavors high-altitude clouds ($\log_{10}P_{\text{cl}} = -1.4^{+1.3}_{-0.6}$ bar) and favors T_{iso} = 850 $^{+120}_{-110}$ K, H₂O (-1.0 $^{+0.4}_{-0.3}$ MMR; -1.9 $^{+0.8}_{-0.6}$ VMR), and a high H₂S abundance (convergence to the upper edge of the prior prevented us from deriving a numerical constraint). Our T_{iso} is compatible within 2- σ with Boucher et al. (2021) and Blain et al. (2024). Our $\log_{10}(\text{H}_2\text{O})$ estimation is in agreement within 1 - σ with Blain et al. (2024) (-1.50 $^{+0.12}_{-0.16}$ in MMR) but twice higher than Boucher et al. (2021) (-4.4 ± 0.4 in VMR). Similarly, our $\log_{10}(\text{H}_2\text{S})$ value (~ 0.1 MMR) is much higher than Fu et al. (2024) (-4.5 $^{+0.57}_{-0.35}$ VMR). This discrepancy may result from our inclusion of more molecular species in the retrieval, resulting in a higher mean molecular weight, a more confined modeled atmosphere, and therefore increased abundances to reach similar line depths. The CCF analysis confirms H₂O at 4.9- σ and tentatively detects H₂S at 3.7- σ with a Kp and V₀ offset toward lower values. Although not favored by the retrieval, we performed a CCF search for CO using Fu et al. (2024)’s abundance and find a 4.4- σ peak at Kp ~ 200 km s⁻¹ and V₀ = -17 km s⁻¹, which we suspect to be driven by uncorrected Rossiter-McLaughlin effect from the host star (Brogi & Line 2019). A combined H₂O+H₂S CCF model yields an unambiguous 5.3- σ detection of the planet atmosphere. We therefore report presence of H₂O, and tentative detections of H₂S and CO. The associated constraints are reported in Table 2.

5.9. HD 209458 b

Discovered in 1999 (Henry et al. 2000), HD 209458 b is a hot Jupiter ($0.68 M_{\text{Jup}}$, $1.36 R_{\text{Jup}}$; Torres et al. (2008)) on a 3.5-day orbit around a G-type star. Prior detections include blueshifted CO (Snellen et al. 2010; Brogi & Line 2019; Giacobbe et al. 2021), H₂O (Sing et al. 2016; Tsiaras et al. 2016b, 2018; Sánchez-López et al. 2019; Giacobbe et al. 2021; Xue et al. 2024), and recent JWST observations reporting CO₂ detection and absence of CH₄, C₂H₂, and HCN (Xue et al. 2024). Our single-transit study converged to a H₂O signature at $K_p = 151_{-24}^{+49}$ km s⁻¹ and $V_0 = -5.7_{-0.9}^{+2.2}$ km s⁻¹, with unconstrained T_{iso} and abundances. These K_p and V_0 values agree well with Sánchez-López et al. (2019) ($K_p = 176_{-38}^{+30}$ km s⁻¹; $V_0 = -5.2_{-1.3}^{+2.6}$ km s⁻¹), yet our CCF search for H₂O only yield a 2.8- σ local peak compatible with a planetary detection but too low even for a tentative detection (Fig. 12). The *Upper Limits Run* mostly rules out $\log_{10}(\text{NH}_3)$ above -3.4 MMR (Table. 3) without improving Xue et al. (2024)'s constraints. We therefore conclude with a non detection of HD 209458 b atmosphere.

5.10. TOI-1807 b

Discovered in 2021 (Hedges et al. 2021), TOI-1807 b is a young planet (~ 300 Myr; $1.26 \pm 0.04 R_{\oplus}$, $2.6 \pm 0.5 M_{\oplus}$; Hedges et al. 2021; Nardiello et al. 2022) on a 0.55-day orbit around a K star. Previous He(2³S) observations reported no atmospheric escape detection (Gaidos et al. 2023; Orell-Miquel et al. 2024; Masson et al. 2024), though absence of He-escape does not rule out primary atmosphere presence, as non-He escape observations have been documented in similar targets with strong H-escape (García Muñoz 2025). We performed here the first molecular signature search for TOI-1807 b to our knowledge, using three SPIRou transits, and obtained puzzling results. The *Full Run analysis* shows clear convergence at $K_p = 164_{-17}^{+25}$ km s⁻¹ (lower than the expected value ~ 220 km s⁻¹) with a redshift of $V_0 \sim 4$ km s⁻¹ (posterior reached prior edge, preventing us from estimating error). The best model yields $T_{\text{iso}} = 2500_{-560}^{+630}$ K, compatible with the $T_{\text{eq}} = 2100_{-40}^{+39}$ estimated by Hedges et al. (2021), and an extremely high H₂S abundance (-0.6 ± 0.2). Computing the CCF map including all species at their median posterior value yield a 4.4- σ tentative signal (Fig. 13), with H₂S alone being tentatively detected at 3.7- σ . As K stars are too hot to contain H₂S, the signal is not of stellar origin. However, the puzzling retrieved constraints call for further verification before claiming this signal as planetary. We performed a phase-dependent CCF analysis (Fig. 6), and obtained a tentative signature appearing only during transit. We further verified whether the signal would be consistent with the expected planetary RV trail using literature parameters ($M_{\star} = 0.76 \pm 0.03 M_{\odot}$, $K_s = 2.39_{-0.46}^{+0.45}$ m s⁻¹, $M_p = 2.6 \pm 0.5 M_{\oplus}$; Nardiello et al. 2022). Taking into account the parameters' error bars, the formula $K_p = K_s \times M_{\star} / M_p$ yields authorized K_p values in the [150–370] km s⁻¹ range, compatible with our retrieved K_p and the tentative signal seen in Fig. 6. Conversely, the V_0 redshift may indicate either an unconstrained eccentricity–plausible in such a young system—or uncertainties in the ephemerides, including potentially unconstrained transiting variations. It is however difficult to consider that we detect any planetary signal considering the extreme H₂S abundance and absence of other detected species. Detailed atmospheric escape and chemistry modeling combined with complementary observations are required to validate or refute this tentative signal, which, if confirmed, would be the first detection of TOI-1807 b's

atmosphere. As these considerations lies outside the scope of this study, we keep them as prospective for future work and report upper limits obtained following the *Upper Limits Run* in Table 3.

5.11. WASP-127 b

Discovered in 2016 (Lam et al. 2017), this hot-Jupiter ($0.16 M_{\text{Jup}}$, $1.3 R_{\text{Jup}}$; Stefansson et al. 2020) orbits a G star on a 3.87-days retrograde, misaligned orbit (Allart et al. 2020). It's highly inflated atmosphere makes it an ideal target for atmospheric studies, with reported detections of H₂O, CO and CO₂ (Welbanks et al. 2019; Spake et al. 2021; Boucher et al. 2023; Nortmann et al. 2025). Nortmann et al. (2025) notably reported a double-peaked CCF consistent with a 7.7 ± 0.2 km s⁻¹ supersonic equatorial jet. Our *Full Run* analysis of the five SPIRou transits (including three from Boucher et al. 2023) converges on an H₂O planetary signal at $K_p = 143.7_{-4.7}^{+5.4}$ km s⁻¹, $V_0 = -6.6_{-0.3}^{+0.4}$ km s⁻¹, $\log_{10}(\text{H}_2\text{O}) = -0.7_{-0.8}^{+0.3}$ MMR ($-1.6_{-1.9}^{+0.8}$ VMR), and $T_{\text{iso}} = 720_{-100}^{+70}$ K (rounded to two significant digits from Fig. 2). We note however that for H₂O convergence near the upper edge of the prior could potentially bias our posterior median and error estimates. The fit favors high-altitude clouds ($\log_{10}(P_{\text{cl}}) = -4.8_{-0.3}^{+0.8}$) and rotational broadening $V_{\text{rot}} = 3.1_{-1.2}^{+1.0}$ km s⁻¹, roughly twice the tidally locked equatorial velocity (~ 1.15 km s⁻¹). The CCF analysis confirms our H₂O signal at 7.5- σ above CCF noise. High-altitude clouds are also favored in previous studies (Skaf et al. 2020; Boucher et al. 2023), and our results agree within 1 - σ confidence intervals with Boucher et al. (2023) ($V_0 = -7.0 \pm 0.5$ km s⁻¹, $\log_{10}(\text{H}_2\text{O}) = -2.39_{-0.63}^{+0.47}$ in VMR, $T_{\text{iso}} = 769_{-253}^{+180}$) and the blueshifted signature in Nortmann et al. (2025). We do not recover the tentative OH signal of Boucher et al. (2023). Our data were not sensitive enough to detect the CO signature and ± 8 km s⁻¹ CCF-splitting reported by Nortmann et al. (2025), though our $\log_{10}(\text{CO})$ posterior ($-3.2_{-3.0}^{+1.9}$ in MMR) would be compatible with their results. We report no detections for the other species and report our constraints in Table 2.

5.12. WASP-69 b

Discovered in 2014, WASP-69 b is a $0.26 M_{\text{Jup}}$, $1.05 R_{\text{Jup}}$ hot Saturn on a 3.87 days orbit around a K star (Anderson et al. 2014). Its large atmospheric scale height allowed for detection of atmospheric escape (e.g., Nortmann et al. 2018; Wang & Dai 2021; Allart et al. 2023; Masson et al. 2024) and molecules such as H₂O, CO, and CO₂ (Tsiaras et al. 2018; Guilluy et al. 2022; Schlawin et al. 2024; Deka et al. 2025). Detections of CH₄, NH₃, and C₂H₂ were reported by Guilluy et al. (2022) from transits observations with GIANO, while Schlawin et al. (2024) found no dayside CH₄ from JWST observations. Analyzing the single SPIRou transit, our *Full Run* analysis converged on a low- K_p H₂O spurious feature that we attribute to telluric residuals. On the other hand, the *Upper Limits Run* favors the presence of CH₄ ($-5.5_{-0.8}^{+0.7}$ in \log_{10} -MMR), HCN ($-4.6_{-0.8}^{+0.7}$), and C₂H₂ ($-4.4_{-0.8}^{+0.7}$), and converged toward the upper edge of the prior for OH ($-0.7_{-0.6}^{+0.3}$) (Fig. 10). Computing a CCF map based on this best model yields a 2.7- σ local maximum compatible with the planetary K_p and $V_0 = 0$ km s⁻¹ yet with too low S/N for even a tentative detection. We therefore report no detection, with upper limits listed in Table 3.

Table 2. *Full Run* retrieval results.

Target	Kp [km s^{-1}]	V_0 [km s^{-1}]	T_{iso} [K]	\log_{10} -MMR									V_{rot} [km s^{-1}]	$\log_{10}(P_{\text{cloud}})$ [bar]
				H ₂ O	CO	CH ₄	NH ₃	CO ₂	H ₂ S	HCN	C ₂ H ₂	OH		
HD 189733 b	138.3 ^{+7.3} _{-7.0}	-3.7 ^{+0.4} _{-0.3}	850 ⁺¹²⁰ ₋₁₁₀	-1.0 ^{+0.4} _{-0.3}	≤ -0.6	≤ -2.8	≤ -2.6	≤ -0.8	-	≤ -1.2	≤ -1.1	≤ -0.6	2.3 ^{+1.1} _{-1.2}	-1.4 ^{+1.3} _{-0.6}
WASP-127 b	143.7 ^{+5.4} _{-4.7}	-6.6 ^{+0.4} _{-0.3}	720 ⁺⁷⁰ ₋₁₀₀	-0.7 ^{+0.3} _{-0.8}	≤ -0.4	≤ -2.0	≤ -2.9	≤ -0.9	≤ -0.8	≤ -1.8	≤ -2.4	≤ -1.1	3.1 ^{+1.0} _{-1.2}	-4.8 ^{+0.8} _{-0.3}
WASP-76 b	214.8 ^{+8.1} _{-8.2}	-9.1 ± 1.0	1530 ⁺²⁸⁰ ₋₂₀₀	-2.5 ± 0.6	-0.8 ^{+0.3} _{-0.7}	≤ -2.3	≤ -3.1	≤ -0.8	≤ -0.7	≤ -2.5	≤ -1.8	≤ -2.3	12.2 ^{+1.6} _{-1.7}	-2.5 ^{+0.7} _{-0.6}
TOI-1807 b*	164 ⁺²⁵ ₋₁₇	-	2480 ⁺⁶³⁰ ₋₅₆₀	≤ -1.8	≤ -0.5	≤ -1.1	≤ -0.7	≤ -1.2	-0.6 ± 0.2	≤ -2.0	≤ -1.4	≤ -1.0	8.8 ^{+3.7} _{-4.9}	0.1 ^{+0.5} _{-0.7}
GJ 3470 b*	128 ⁺¹⁷ ₋₁₆	-5.4 ± 0.8	1100 ⁺⁷⁰ ₋₁₀₀	≤ -2.4	≤ -0.5	-1.4 ^{+0.5} _{-0.6}	≤ -2.4	≤ -1.0	≤ -0.9	≤ -1.9	≤ -1.7	-	4.0 ^{+1.7} _{-1.9}	-0.5 ^{+1.0} _{-1.2}

Notes. Results obtained from the *Full Run* analysis. Values are given as median posteriors with 1- σ uncertainties. Upper limits are given at the 3- σ level. Errors were further pessimistically rounded to a maximum of 2 digits. Targets marked with an * correspond to tentative atmospheric detections.

Table 3. *Upper Limits Run* results.

Target	H ₂ O	CO	CH ₄	NH ₃	CO ₂	H ₂ S	HCN	C ₂ H ₂	OH
55 CnC e	-1.9	-0.1	-0.2	-	-	-0.3	-	-0.5	-0.1
AU Mic b	-1.7	-0.3	-3.1	-3.6	-0.1	-1.4	-0.7	-2.4	-0.5
GJ 1214 b	-	-0.6	-5.1	-5.7	-3.3	-4.4	-3.7	-3.6	-1.3
GJ 3470 b	-3.1	-0.1	-1.9	-5.7	-3.1	-3.2	-4.5	-4.3	-
GJ 486 b	-1.4	-	-0.1	-4.4	-0.3	-0.3	-2.5	-3.3	-0.2
HAT-P-11 b	-0.4	-	-	-3.3	-	-	-0.5	-0.1	-
HD 209458 b	-0.7	-	-	-3.4	-0.1	-0.4	-0.2	-0.5	-
TOI-1807 b	-0.8	-	-0.3	-	-	-	-	-0.3	-0.1
WASP-69 b	-2.2	-0.2	-1.2	-4.8	-1.5	-4.1	-2.4	-1.6	-0.1
WASP-80 b	-	-0.4	-1.9	-4.0	-0.1	-	-0.4	-0.1	-

Notes. 3- σ upper limits obtained from the *Upper Limits Run* (Sec. 4.1). No constraints could be obtained for GJ 436 b. The priors on \log_{10} -MMR were set to be uniform over the [-8 - 0] range (Tab. 5).

5.13. WASP-76 b

Discovered in 2016 (West et al. 2016), this ultrahot Jupiter (0.9 M_{Jup} , 1.85 R_{Jup} ; Ehrenreich et al. 2020) orbits a F star in 1.8 days. Previous studies reported potential atmospheric escape (Casasayas-Barris et al. 2021; Lampón et al. 2023; Masson et al. 2024) and molecular detections of H₂O, CO, OH, HCN, TiO, and VO (Tsiaras et al. 2018; Landman et al. 2021; Fu et al. 2021; Sánchez-López et al. 2022; Yan et al. 2023; Maguire et al. 2024; Hood et al. 2024; Gandhi et al. 2024, e.g.). Ehrenreich et al. (2020) notably reported asymmetric CCF-detection of Fe attributed to nightside iron-clouds condensation. Hood et al. (2024)'s SPIRou retrieval disfavors clouds above 10⁻⁴ bar and resulted in H₂O and CO detections at different Kp values which they attribute to atmospheric circulation. We analyzed three SPIRou transits (including the 2020-10-31 observation of Hood et al. 2024). The *Full Run* shows clear convergence to H₂O and CO at Kp = 214.8^{+8.1}_{-8.2} km s^{-1} and $V_0 = -9.1 \pm 1.0$ km s^{-1} , with $\log_{10}(\text{H}_2\text{O}) = -2.5 \pm 0.6$ MMR (-3.3 ± 0.8 VMR) and $\log_{10}(\text{CO}) = -0.8^{+0.3}_{-0.7}$ MMR (-1.7^{+0.8}_{-1.5} VMR) (Fig. 8). The best model yields $T_{\text{iso}} = 1530^{+280}_{-200}$ K, substantial rotational broadening $V_{\text{rot}} = 12.2^{+1.6}_{-1.7}$ km s^{-1} , and high-altitude clouds at $\log_{10}P_{\text{cl}} = -2.5^{+0.7}_{-0.6}$ bar. From the CCF analysis, the H₂O signal is confirmed at 5.6- σ while the CO signature is tentatively detected at 3.6- σ . Our abundances are consistent with Sánchez-López et al. (2022) and slightly exceed Hood et al. (2024)'s cloud-free results, which is expected given our model's preference for high-altitude clouds

and therefore the need for higher abundances to fit the same signal. We estimated the C/O ratio to be nearly solar (C/O ~ 1), but uncertainties in the H₂O and CO abundances prevent us from concluding toward a super- or sub-solar C/O value. Other species were not detected, and we report our constraints in Table 2.

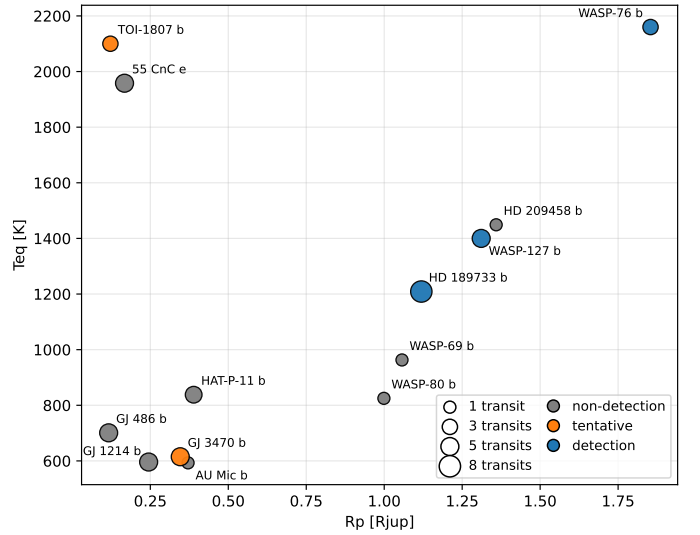


Fig. 3. Radius–equilibrium temperature summary diagram of the 14 targets. Marker size scales with the number of analyzed transits, and colors indicate whether an atmosphere was detected (blue), tentatively detected (orange), and non-detected (gray).

5.14. WASP-80 b

WASP-80 b (0.54 M_{Jup} , ~ 1 R_{Jup} ; Triaud et al. 2013, 2015) is a warm Jupiter on a 3-day orbit around a relatively active K star. No atmospheric escape has been detected (Fossati et al. 2022, 2023; Allart et al. 2023; Masson et al. 2024), despite predictions for strong escape (Salz et al. 2016). Prior work reported detections of H₂O, CO, CH₄, NH₃, HCN, and tentative CO₂ (Carleo et al. 2022; Bell et al. 2023; Jacobs et al. 2023). Our single SPIRou transit lacks the sensitivity to independently confirm these detections. The *Full Run* converges on a spurious telluric-driven H₂O signature, while the *Upper Limits Run* yields unrealistically high H₂O abundances (attributed to telluric residuals) and marginal C₂H₂ at $\log_{10}(\text{C}_2\text{H}_2) = -2.3^{+0.9}_{-1.5}$, unconfirmed by CCF analysis. We therefore report no atmospheric detection and provide upper limits in Table 3.

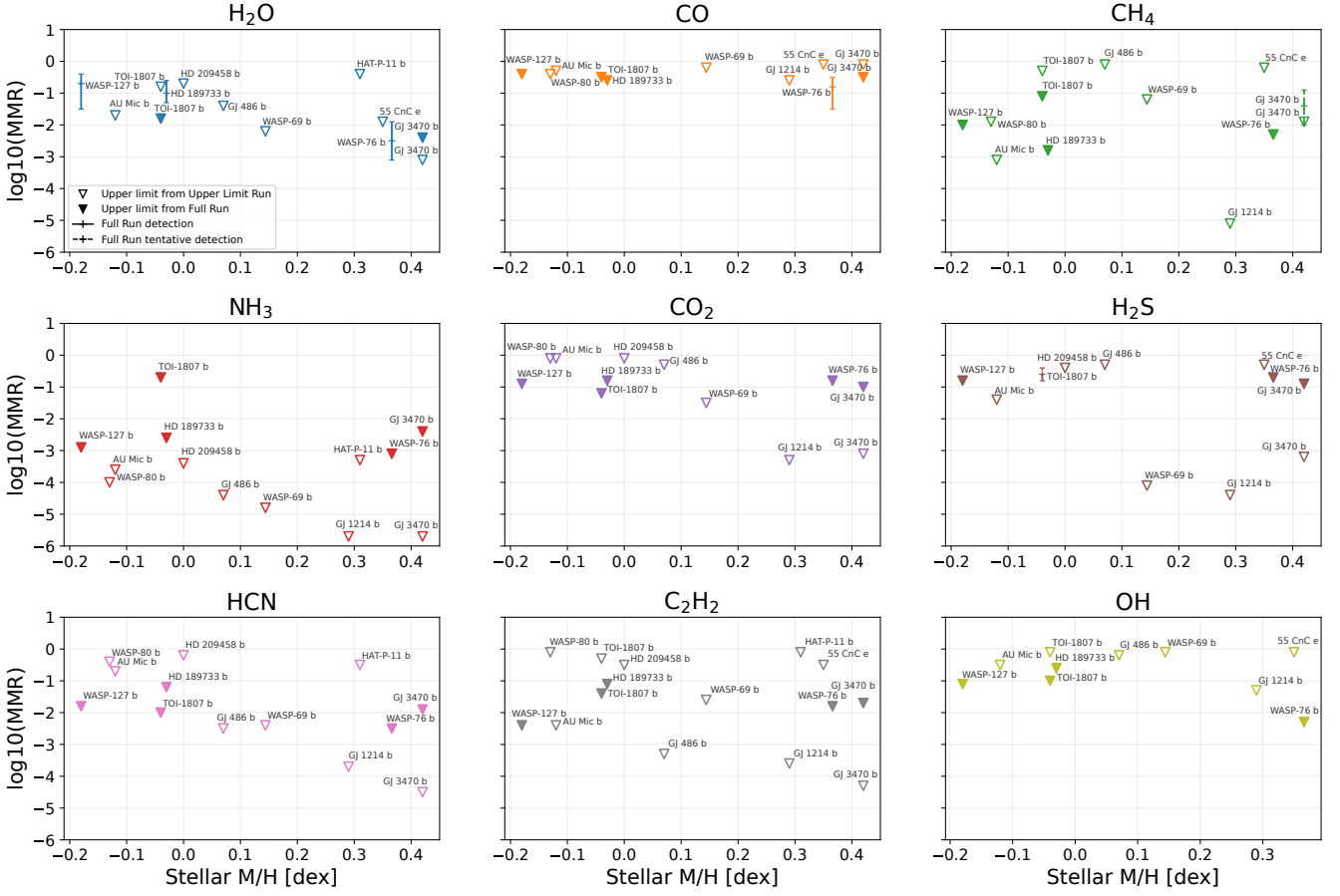


Fig. 4. Constraints obtained on $\log_{10}(\text{MMR})$ for each target as a function of host-star metallicity (log scale, relative to solar). Upper limits are shown as open and filled triangles for the *Upper Limits Run* and *Full Run*, respectively. Constraints from the *Full Run* are shown with solid and dashed error bars for robust and tentative atmospheric detections, respectively. Error bars and upper limits correspond to the 1- σ and 3- σ uncertainties reported in Tables 2 and 3. Note that TOI-1807 b and GJ 3470 b display two sets of constraints in some subplots: one from the *Full Run*, and one from the *Upper Limits Run*.

5.15. Results overview

Our results from the *Full Run* and *Upper Limits Run* are compiled in Tables 2 and 3, respectively. For visualization, we provide a summary figure showing the atmospheric detection status of each target as a function of the number of combined transits in the radius–equilibrium temperature plane (Fig. 3). Unambiguous atmospheric detections are achieved only for hot-Jupiter targets with at least three combined transits, highlighting the need to stack additional observations to reach detection thresholds for other systems. To search for population trends, we derived the ranges of C/O, H₂O/H, and atmospheric metallicity permitted by the constraints obtained for each target in both runs. Plotting these quantities as a function of host-star metallicity or equilibrium temperature does not reveal a clear population-level trend, mainly because most upper limits remain weakly constraining. Reaching a level of precision suitable for robust population studies will require additional observations and complementary wavelength coverage. The derived MMR constraints per target as a function of host-star metallicity are shown in Fig. 4, while additional figures are available as supplementary material in the associated repository¹⁰. Although no clear correlation is inferred, these figures provide a useful overview of the sensitiv-

ity of our retrieval framework to each molecule: NH₃ is generally the most strongly constrained species (i.e., with the lowest upper limits), likely because of its dense line forest in the SPIRou wavelength range and its negligible contribution in Earth’s atmosphere and M-dwarf spectra. By contrast, H₂O, CO, CO₂, and OH are the most challenging species to constrain, likely because of stronger telluric contamination and, for M-dwarf hosts, residual stellar contamination.

6. Summary and Conclusions

We conducted a global analysis of 50 observations of 14 transiting exoplanets obtained with SPIRou at CFHT, combining public PI-archival data with data from three large programs (ATMOSPHERIX, SLS, SPICE). We developed an automated pipeline for the homogeneous reduction and analysis of large ground-based high-resolution spectroscopy datasets for atmospheric characterization, including a novel, unbiased automated optimization of SysRem or PCA for correlated residuals correction.

We performed a blind-search for nine molecules across all targets, using Nested Sampling retrievals cross-validated with Cross Correlation Function (CCF) analyses. We detect H₂O and a tentative CO signal in HD 189733 b, H₂O in WASP-127 b, and H₂O with a tentative CO signal in WASP-76 b, in agreement with

¹⁰ See Fig. 18 to 20 on <https://cloud.cab.inta-csic.es/s/Ss7GDRbzx6MySNZ>

previous studies. These robust detections allowed us to constrain orbital radial velocity, atmospheric temperature, cloud pressure deck, and atmospheric circulation. While these constraints rely on strong model assumptions due to computational limitations, their consistency with prior work validates our automated blind-search approach for the remainder of the dataset.

We also report several unexpected, potentially spurious, tentative signals that warrant further investigation. We find a tentative $3.7\text{-}\sigma$ H_2S signature in HD 189733 b which may support recent JWST observations. For GJ 3470 b, we identify a tentative OH signal at $4.3\text{-}\sigma$, although its planetary origin cannot be unambiguously distinguished from residual stellar contamination from the M-dwarf host. Finally, we detect a tentative $4.4\text{-}\sigma$ signal in TOI-1807 b using a model including all species at their best posterior values, with H_2S alone producing a tentative $3.7\text{-}\sigma$ signal. The location of the CCF peak in (K_p , V_0) space is compatible with a planetary origin given current orbital uncertainties and, if confirmed, could indicate a slight eccentricity. However, assessing the physical plausibility of the inferred atmospheric properties will require further theoretical exploration beyond the scope of this work. At the population scale, our comparative analysis does not reveal any clear trend, mainly due to weakly informative upper limits. Additional observations, combined with complementary wavelength coverage, will be necessary to obtain constraints suitable for population-level analyses.

The pipeline and methodology presented here are scalable to larger planetary samples and readily adaptable to other ground-based high-resolution spectrographs. As ground-based high-resolution spectroscopy provides a critical complement to space-based observations, efficient and automated reduction and analysis frameworks are becoming essential to keep pace with the increasing scale and ambition of atmospheric characterization efforts. Continued development is underway to improve telluric and stellar correction, reduce computational costs, and enable more complex atmospheric models in preparation for upcoming facilities and missions such as Ariel and ANDES.

Acknowledgments

This research has been funded by the grants n° CNS2023-144309 by the Spain Ministry of Science, Innovation and Universities (MICIU/AEI/10.13039/501100011033) and NextGenerationEU/PRTR grants CNS2023-144309 and PID2023-150468NB-I00. V. Yariv acknowledges funding from the physics doctoral school (ED-PHYS) of the Grenoble-Alpes University. F. Debras acknowledges fundings from the French National Research Agency (ANR) project ExoATMO (ANR-25-CE49-6598), the *Action Thématique Physique Stellaire* (ATPS), and the *Action Thématique ExoSystèmes* (AT-EXOS) of CNRS/INSU co-funded by CEA and CNES. R. Allart acknowledges the Swiss National Science Foundation (SNSF) support under the Post-Doc Mobility grant P500PT_222212 and the support of the Institut Trottier de Recherche sur les Exoplanètes (IREx). This work is based on observations obtained at the Canada-France-Hawaii Telescope (CFHT) which is operated from the summit of Maunakea by the National Research Council of Canada, the Institut National des Sciences de l'Univers of the Centre National de la Recherche Scientifique of France, and the University of Hawaii. The observations at the Canada-France-Hawaii Telescope were performed with care and respect from the summit of Maunakea which is a significant cultural and historic site. This work has made use of the NASA Exoplanet Archive (exoplanetarchive.ipac.caltech.edu), The Extrasolar Planets Encyclopaedia (exoplanet.eu), the Astrophysics Data

System (ui.adsabs.harvard.edu), and the SIMBAD database (simbad.u-strasbg.fr). This work has made use of the following Python packages: Numpy (Harris et al. 2020); SciPy (Virtanen et al. 2020); Astropy (Astropy Collaboration et al. 2013, 2018, 2022); PyAstronomy (Czesla et al. 2019); statsmodel (Seabold & Perktold 2010); Jupyter (Granger & Pérez 2021); Matplotlib (Hunter 2007); PyMultinest (Buchner et al. 2014); batman (Kreidberg 2015); petitRADTRANS (Mollière et al. 2019); and Exo-REM (Baudino et al. 2015, 2017; Charnay et al. 2018; Blain et al. 2021).

References

- Ahn, S. & Fessler, A. 2003, Standard Errors of Mean, Variance, and Standard Deviation Estimators, Tech. rep., Technical Report, Ann Arbor, MI, USA
- Alei, E., Konrad, B. S., Angerhausen, D., et al. 2022, *A&A*, 665, A106
- Allart, R., Bourrier, V., Lovis, C., et al. 2018, *Science*, 362, 1384
- Allart, R., Lemée-Joliecoeur, P. B., Jaziri, A. Y., et al. 2023, *A&A*, 677, A164
- Allart, R., Pino, L., Lovis, C., et al. 2020, *A&A*, 644, A155
- Alonso-Floriano, F. J., Sánchez-López, A., Snellen, I. A. G., et al. 2019, *A&A*, 621, A74
- Anderson, D. R., Collier Cameron, A., Delrez, L., et al. 2014, *MNRAS*, 445, 1114
- Angelo, I. & Hu, R. 2017, *AJ*, 154, 232
- Artigau, É., Saint-Antoine, J., Lévesque, P.-L., et al. 2018, in Society of Photo-Optical Instrumentation Engineers (SPIE) Conference Series, Vol. 10709, High Energy, Optical, and Infrared Detectors for Astronomy VIII, ed. A. D. Holland & J. Beletic, 107091P
- Astropy Collaboration, Price-Whelan, A. M., Lim, P. L., et al. 2022, *apj*, 935, 167
- Astropy Collaboration, Price-Whelan, A. M., Sipőcz, B. M., et al. 2018, *AJ*, 156, 123
- Astropy Collaboration, Robitaille, T. P., Tollerud, E. J., et al. 2013, *A&A*, 558, A33
- Bakos, G. Á., Torres, G., Pál, A., et al. 2010, *ApJ*, 710, 1724
- Basilicata, M., Giacobbe, P., Bonomo, A. S., et al. 2024, *A&A*, 686, A127
- Baudino, J. L., Bézard, B., Boccaletti, A., et al. 2015, *A&A*, 582, A83
- Baudino, J.-L., Mollière, P., Venot, O., et al. 2017, *ApJ*, 850, 150
- Bean, J. L., Désert, J.-M., Kabath, P., et al. 2011, *ApJ*, 743, 92
- Bean, J. L., Miller-Ricci Kempton, E., & Homeier, D. 2010, *Nature*, 468, 669
- Beatty, T. G., Welbanks, L., Schlawin, E., et al. 2024, *ApJ*, 970, L10
- Bell, T. J., Welbanks, L., Schlawin, E., et al. 2023, *Nature*, 623, 709
- Benneke, B., Knutson, H. A., Lothringer, J., et al. 2019, *Nature Astronomy*, 3, 813
- Berta, Z. K., Charbonneau, D., Désert, J.-M., et al. 2012, *ApJ*, 747, 35
- Birkby, J. L., de Kok, R. J., Brogi, M., et al. 2013, *MNRAS*, 436, L35
- Birkby, J. L., de Kok, R. J., Brogi, M., Schwarz, H., & Snellen, I. A. G. 2017, *The Astronomical Journal*, 153, 138
- Blain, D., Charnay, B., & BÀ©zard, B. 2021, 646, A15
- Blain, D., Sánchez-López, A., & Mollière, P. 2024, *AJ*, 167, 179
- Bonfils, X., Gillon, M., Udry, S., et al. 2012, *A&A*, 546, A27
- Boucher, A., Darveau-Bernier, A., Pelletier, S., et al. 2021, *AJ*, 162, 233
- Boucher, A., Lafrenière, D., Pelletier, S., et al. 2023, *MNRAS*, 522, 5062
- Bouchy, F., Udry, S., Mayor, M., et al. 2005, *A&A*, 444, L15
- Bourrier, V., Dumusque, X., Dorn, C., et al. 2018, *A&A*, 619, A1
- Brogi, M., Giacobbe, P., Guilluy, G., et al. 2018, *A&A*, 615, A16
- Brogi, M. & Line, M. R. 2019, *AJ*, 157, 114
- Buchner, J., Georgakakis, A., Nandra, K., et al. 2014, *A&A*, 564, A125
- Butler, R. P., Vogt, S. S., Marcy, G. W., et al. 2004, *ApJ*, 617, 580
- Caballero, J. A., González-Álvarez, E., Brady, M., et al. 2022, *A&A*, 665, A120
- Cabot, S. H. C., Madhusudhan, N., Hawker, G. A., & Gandhi, S. 2019, *MNRAS*, 482, 4422
- Carleo, I., Giacobbe, P., Guilluy, G., et al. 2022, *AJ*, 164, 101
- Carvalho, A. & Johns-Krull, C. M. 2023, *Research Notes of the American Astronomical Society*, 7, 91
- Casasayas-Barris, N., Palle, E., Stangret, M., et al. 2021, *A&A*, 647, A26
- Chachan, Y., Knutson, H. A., Gao, P., et al. 2019, *The Astronomical Journal*, 158, 244
- Charbonneau, D., Berta, Z. K., Irwin, J., et al. 2009, *Nature*, 462, 891
- Charnay, B., Bézard, B., Baudino, J. L., et al. 2018, *ApJ*, 854, 172
- Cheverall, C. J., Madhusudhan, N., & Holmberg, M. 2023, *MNRAS*, 522, 661
- Chiavassa, A. & Brogi, M. 2019, *A&A*, 631, A100
- Choi, Y.-H., Jeong, U., Lee, J.-J., et al. 2025, *AJ*, 170, 238
- Cleveland, W. S. 1979, *Journal of the American Statistical Association*, 74, 829
- Cloutier, R., Charbonneau, D., Deming, D., Bonfils, X., & Astudillo-Defru, N. 2021, *AJ*, 162, 174
- Cook, N. J., Artigau, É., Doyon, R., et al. 2022, *PASP*, 134, 114509

- Crossfield, I. J. M., Barman, T., Hansen, B. M. S., & Howard, A. W. 2013, *A&A*, 559, A33
- Cubillos, P. E., Harrington, J., Blecic, J., et al. 2022, *The Planetary Science Journal*, 3, 81
- Czesla, S., Schröter, S., Schneider, C. P., et al. 2019, PyA: Python astronomy-related packages
- Dash, S., Brogi, M., Gandhi, S., et al. 2024, *MNRAS*, 530, 3100
- Dawson, R. I. & Fabrycky, D. C. 2010, *ApJ*, 722, 937
- de Mooij, E. J. W., Brogi, M., de Kok, R. J., et al. 2012, *A&A*, 538, A46
- Debras, F., Klein, B., Donati, J.-F., et al. 2024, *MNRAS*, 527, 566
- Deibert, E. K., de Mooij, E. J. W., Jayawardhana, R., et al. 2021, *AJ*, 161, 209
- Deka, T., Majumdar, L., Basra Khan, T., et al. 2025, arXiv e-prints, arXiv:2510.27223
- Demory, B.-O., Gillon, M., de Wit, J., et al. 2016, *Nature*, 532, 207
- Désert, J.-M., Bean, J., Miller-Ricci Kempton, E., et al. 2011, *ApJ*, 731, L40
- Donati, J.-F., Kouach, D., Lacombe, M., et al. 2018, in *Handbook of Exoplanets*, ed. H. J. Deeg & J. A. Belmonte, 107
- Donati, J. F., Kouach, D., Moutou, C., et al. 2020, *MNRAS*, 498, 5684
- dos Santos, L. A., Ehrenreich, D., Bourrier, V., et al. 2019, *A&A*, 629, A47
- Dos Santos, L. A., Vidotto, A. A., Vissapragada, S., et al. 2022, *A&A*, 659, A62
- Dragomir, D., Benneke, B., Pearson, K. A., et al. 2015, *ApJ*, 814, 102
- Eastman, J., Siverd, R., & Gaudi, B. S. 2010, *PASP*, 122, 935
- Ehrenreich, D., Bourrier, V., Bonfils, X., et al. 2012, *A&A*, 547, A18
- Ehrenreich, D., Bourrier, V., Wheatley, P. J., et al. 2015, *Nature*, 522, 459
- Ehrenreich, D., Lovis, C., Allart, R., et al. 2020, *Nature*, 580, 597
- Esteves, L. J., de Mooij, E. J. W., Jayawardhana, R., Watson, C., & de Kok, R. 2017, *The Astronomical Journal*, 153, 268
- Feroz, F. & Hobson, M. P. 2008, *Monthly Notices of the Royal Astronomical Society*, 384, 449
- Feroz, F., Hobson, M. P., Cameron, E., & Pettitt, A. N. 2019, *The Open Journal of Astrophysics*, 2, 10
- Fossati, L., Guilluy, G., Shaikhislamov, I. F., et al. 2022, *A&A*, 658, A136
- Fossati, L., Pillitteri, I., Shaikhislamov, I. F., et al. 2023, *A&A*, 673, A37
- Fraine, J., Deming, D., Benneke, B., et al. 2014, *Nature*, 513, 526
- Fu, G., Deming, D., Lothringer, J., et al. 2021, *AJ*, 162, 108
- Fu, G., Welbanks, L., Deming, D., et al. 2024, *Nature*, 632, 752
- Gaidos, E., Hirano, T., Lee, R. A., et al. 2023, *MNRAS*, 518, 3777
- Gandhi, S., Brogi, M., & Webb, R. K. 2020, *MNRAS*, 498, 194
- Gandhi, S., Landman, R., Snellen, I., et al. 2024, *MNRAS*, 530, 2885
- García Muñoz, A. 2025, *A&A*, 698, A199
- Giacobbe, P., Brogi, M., Gandhi, S., et al. 2021, *Nature*, 592, 205
- Gibson, N. P., Nugroho, S. K., Lothringer, J., Maguire, C., & Sing, D. K. 2022, *MNRAS*, 512, 4618
- Granger, B. E. & Pérez, F. 2021, *Computing in Science & Engineering*, 23, 7
- Grasser, N., Snellen, I. A. G., Landman, R., Picos, D. G., & Gandhi, S. 2024, *A&A*, 688, A191
- Guilluy, G., Giacobbe, P., Carleo, I., et al. 2022, *A&A*, 665, A104
- Hargreaves, R. J., Gordon, I. E., Rey, M., et al. 2020, *ApJS*, 247, 55
- Harris, C. R., Millman, K. J., van der Walt, S. J., et al. 2020, *Nature*, 585, 357
- Harris, G. J., Tennyson, J., Kaminsky, B. M., Pavlenko, Y. V., & Jones, H. R. A. 2006, *MNRAS*, 367, 400
- Hedges, C., Hughes, A., Zhou, G., et al. 2021, *AJ*, 162, 54
- Helling, C., Woitke, P., Rimmer, P. B., et al. 2014, *Life*, 4, 142
- Henry, G. W., Marcy, G. W., Butler, R. P., & Vogt, S. S. 2000, *ApJ*, 529, L41
- Hood, T., Debras, F., Moutou, C., et al. 2024, arXiv e-prints, arXiv:2403.19434
- Hu, R., Bello-Arufe, A., Zhang, M., et al. 2024, arXiv e-prints, arXiv:2405.04744
- Huber, K. F., Czesla, S., & Schmitt, J. H. M. M. 2017, *A&A*, 597, A113
- Hunter, J. D. 2007, *Computing in Science & Engineering*, 9, 90
- Jacobs, B., Désert, J.-M., Gao, P., et al. 2023, *ApJ*, 956, L43
- Keles, E., Mallonn, M., Kitzmann, D., et al. 2022, *MNRAS*, 513, 1544
- Kesseli, A. Y., Snellen, I. A. G., Alonso-Floriano, F. J., Mollière, P., & Serindag, D. B. 2020, *AJ*, 160, 228
- Klein, B., Debras, F., Donati, J.-F., et al. 2024, *MNRAS*, 527, 544
- Kokori, A., Tsiaras, A., Edwards, B., et al. 2023, *ApJS*, 265, 4
- Kokori, A., Tsiaras, A., Edwards, B., et al. 2022a, *ApJS*, 258, 40
- Kokori, A., Tsiaras, A., Edwards, B., et al. 2022b, *Experimental Astronomy*, 53, 547
- Kosiarek, M. R., Crossfield, I. J. M., Hardegree-Ullman, K. K., et al. 2019, *AJ*, 157, 97
- Kreidberg, L. 2015, 127, 1161
- Kreidberg, L., Bean, J. L., Désert, J.-M., et al. 2014, *Nature*, 505, 69
- Kulow, J. R., France, K., Linsky, J., & Loyd, R. O. P. 2014, *ApJ*, 786, 132
- Lam, K. W. F., Faedi, F., Brown, D. J. A., et al. 2017, *A&A*, 599, A3
- Lampón, M., López-Puertas, M., Sanz-Forcada, J., et al. 2023, arXiv e-prints, arXiv:2304.03839
- Landman, R., Sánchez-López, A., Mollière, P., et al. 2021, *A&A*, 656, A119
- Lavie, B., Ehrenreich, D., Bourrier, V., et al. 2017, *A&A*, 605, L7
- Line, M. R., Knutson, H., Wolf, A. S., & Yung, Y. L. 2014, *ApJ*, 783, 70
- Madhusudhan, N. & Seager, S. 2011, *ApJ*, 729, 41
- Maguire, C., Gibson, N. P., Nugroho, S. K., et al. 2024, *A&A*, 687, A49
- Mamajek, E. E. & Bell, C. P. M. 2014, *MNRAS*, 445, 2169
- Marboeuf, U., Thiabaud, A., Alibert, Y., Cabral, N., & Benz, W. 2014, *A&A*, 570, A35
- Masson, A., Vinatier, S., Bézard, B., et al. 2024, *A&A*, 688, A179
- Maxted, P. F. L., Ehrenreich, D., Wilson, T. G., et al. 2022, *MNRAS*, 514, 77
- Mazeh, T., Tamuz, O., & Zucker, S. 2007, in *Astronomical Society of the Pacific Conference Series*, Vol. 366, *Transiting Extrapolar Planets Workshop*, ed. C. Afonso, D. Weldrake, & T. Henning, 119
- McArthur, B. E., Endl, M., Cochran, W. D., et al. 2004, *ApJ*, 614, L81
- McLaughlin, D. B. 1924, *ApJ*, 60, 22
- Mercier, S. J., Dang, L., Gass, A., Cowan, N. B., & Bell, T. J. 2022, *AJ*, 164, 204
- Miller-Ricci Kempton, E., Zahnle, K., & Fortney, J. J. 2012, *ApJ*, 745, 3
- Mollière, P., Stolker, T., Lacour, S., et al. 2020, *A&A*, 640, A131
- Mollière, P., Wardenier, J. P., van Boekel, R., et al. 2019, *A&A*, 627, A67
- Moran, S. E., Stevenson, K. B., Sing, D. K., et al. 2023, *ApJ*, 948, L11
- Moses, J. I., Madhusudhan, N., Visscher, C., & Freedman, R. S. 2013, *ApJ*, 763, 25
- Nardiello, D., Malavolta, L., Desidera, S., et al. 2022, *A&A*, 664, A163
- Nascimben, V., Piotto, G., Pagano, I., et al. 2013, *A&A*, 559, A32
- Nasedkin, E., Mollière, P., & Blain, D. 2024, *The Journal of Open Source Software*, 9, 5875
- Ninan, J. P., Stefansson, G., Mahadevan, S., et al. 2020, *ApJ*, 894, 97
- Nortmann, L., Lesjak, F., Yan, F., et al. 2025, *A&A*, 693, A213
- Nortmann, L., Pallé, E., Salz, M., et al. 2018, *Science*, 362, 1388
- Nugroho, S. K., Kawahara, H., Gibson, N. P., et al. 2021, *ApJ*, 910, L9
- Öberg, K. I., Murray-Clay, R., & Bergin, E. A. 2011, *ApJ*, 743, L16
- Orell-Miquel, J., Murgas, F., Pallé, E., et al. 2024, arXiv e-prints, arXiv:2404.16732
- Palle, E., Nortmann, L., Casasayas-Barris, N., et al. 2020a, *A&A*, 638, A61
- Palle, E., Oshagh, M., Casasayas-Barris, N., et al. 2020b, *A&A*, 643, A25
- Plavchan, P., Barclay, T., Gagné, J., et al. 2020, *Nature*, 582, 497
- Rasmussen, K. C., Currie, M. H., Hagee, C., et al. 2023, arXiv e-prints, arXiv:2308.10378
- Ridden-Harper, A., Nugroho, S. K., Flagg, L., et al. 2023, *AJ*, 165, 170
- Ridden-Harper, A. R., Snellen, I. A. G., Keller, C. U., et al. 2016, *A&A*, 593, A129
- Rockcliffe, K. E., Newton, E. R., Youngblood, A., et al. 2023, *AJ*, 166, 77
- Rothman, L., Gordon, I., Barber, R., et al. 2010, *Journal of Quantitative Spectroscopy and Radiative Transfer*, 111, 2139, xVIlth Symposium on High Resolution Molecular Spectroscopy (HighRes-2009)
- Rothman, L. S., Gordon, I. E., Babikov, Y., et al. 2013, *J. Quant. Spectr. Rad. Transf.*, 130, 4
- Salz, M., Schneider, P. C., Czesla, S., & Schmitt, J. H. M. M. 2016, *A&A*, 585, L2
- Sánchez-López, A., Alonso-Floriano, F. J., López-Puertas, M., et al. 2019, *A&A*, 630, A53
- Sánchez-López, A., Landman, R., Mollière, P., et al. 2022, *A&A*, 661, A78
- Satopaa, V., Albrecht, J., Irwin, D., & Raghavan, B. 2011, 166
- Schlawin, E., Mukherjee, S., Ohno, K., et al. 2024, *AJ*, 168, 104
- Seabold, S. & Perktold, J. 2010, *Proceedings of the 9th Python in Science Conference*, 2010
- Sing, D. K., Fortney, J. J., Nikolov, N., et al. 2016, *Nature*, 529, 59
- Skaif, N., Bieger, M. F., Edwards, B., et al. 2020, *AJ*, 160, 109
- Snellen, I. A. G., Albrecht, S., de Mooij, E. J. W., & Le Poole, R. S. 2008, *A&A*, 487, 357
- Snellen, I. A. G., de Kok, R. J., de Mooij, E. J. W., & Albrecht, S. 2010, *Nature*, 465, 1049
- Spake, J. J., Sing, D. K., Wakeford, H. R., et al. 2021, *MNRAS*, 500, 4042
- Stefansson, G., Mahadevan, S., Maney, M., et al. 2020, *AJ*, 160, 192
- Stevenson, K. B., Harrington, J., Nymeyer, S., et al. 2010, *Nature*, 464, 1161
- Swain, M. R., Vasisth, G., Tinetti, G., et al. 2009, *ApJ*, 690, L114
- Tabernero, H. M., Zapatero Osorio, M. R., Allart, R., et al. 2021, *A&A*, 646, A158
- Tamuz, O., Mazeh, T., & Zucker, S. 2005, 356, 1466
- Teske, J. K., Turner, J. D., Mueller, M., & Griffith, C. A. 2013, *MNRAS*, 431, 1669
- Tinetti, G., Drossart, P., Eccleston, P., et al. 2018, *Experimental Astronomy*, 46, 135
- Torres, G., Winn, J. N., & Holman, M. J. 2008, *ApJ*, 677, 1324
- Triaud, A. H. M. J., Anderson, D. R., Collier Cameron, A., et al. 2013, *A&A*, 551, A80
- Triaud, A. H. M. J., Gillon, M., Ehrenreich, D., et al. 2015, *MNRAS*, 450, 2279
- Trifonov, T., Caballero, J. A., Morales, J. C., et al. 2021, *Science*, 371, 1038
- Tsiaras, A., Rocchetto, M., Waldmann, I. P., et al. 2016a, *ApJ*, 820, 99
- Tsiaras, A., Waldmann, I. P., Rocchetto, M., et al. 2016b, *ApJ*, 832, 202
- Tsiaras, A., Waldmann, I. P., Zingales, T., et al. 2018, *AJ*, 155, 156
- Turrini, D., Codella, C., Danielski, C., et al. 2022, *Experimental Astronomy*, 53, 225
- Valencia, D., Guillot, T., Parmentier, V., & Freedman, R. S. 2013, *ApJ*, 775, 10
- Virtanen, P., Gommers, R., Oliphant, T. E., et al. 2020, *Nature Methods*, 17, 261
- Wang, L. & Dai, F. 2021, *ApJ*, 914, 98
- Welbanks, L., Madhusudhan, N., Allard, N. F., et al. 2019, *ApJ*, 887, L20
- West, R. G., Hellier, C., Almenara, J. M., et al. 2016, *A&A*, 585, A126
- Wright, J. T. & Eastman, J. D. 2014, *PASP*, 126, 838
- Xue, Q., Bean, J. L., Zhang, M., et al. 2024, *ApJ*, 963, L5
- Yan, F., Nortmann, L., Reinert, A., et al. 2023, *A&A*, 672, A107
- Yang, Y., Chen, G., Zhang, H., & Yan, F. 2025, *A&A*, 703, A39
- Zhang, M., Knutson, H. A., Wang, L., et al. 2021, *AJ*, 161, 181
- Zicher, N., Barragán, O., Klein, B., et al. 2022, *MNRAS*, 512, 3060

Appendix

6.1. Sigma clipping

Once cleaned with SysRem, we apply a last sigma clipping step to remove any remaining outliers that may have survived or arised during the previous reduction steps (e.g., extreme values resulting from the division by an almost null value). This time, our rejection criterion is based on the spectral distribution of the individual spectral bins' error σ_{λ_i} , approximated as the standard deviation of each spectral bin λ_i along the time axis. How much the $\{\sigma_{\lambda_i}\}_{i=1}^{N_\lambda}$ (with N_λ the number of spectral bins) are dispersed around the true $\sigma(\lambda)$ statistic is determined by the standard error SE_σ , whose expression can be approximated as (see, e.g., eq. 3 in [Ahn & Fessler 2003](#)):

$$SE_\sigma = \frac{\sigma(\lambda)}{\sqrt{2(N_{obs} - 1)}} \quad (2)$$

With N_{obs} the number of observed exposures. Since we do not have access to the true $\sigma(\lambda)$ statistic, we approximated it by fitting the $\{\sigma_{\lambda_i}\}$ distribution with a LOWESS¹¹ function (locally weighted scatterplot smoothing; [Cleveland 1979](#)), which uses local linear regression to fit a smooth curve to a set of data points with low sensitivity to outliers. We empirically set the rolling fitting window to comprise 20% of the data, and found this method to yield a better fit than classical polynomial models. We further added an Earth atmospheric transmission correction term $T(\lambda)$ to account for the fact that spectral bins lying in low-transmission ranges would exhibit a higher noise level without necessarily being outliers. Replacing $\sigma(\lambda)$ by it's approximated values from the LOWESS fit $\mathcal{L}(\lambda)$ in eq. 2, our final rejection criterion for each spectral bin λ_i can be written as:

$$|\sigma_{\lambda_i} - \frac{\mathcal{L}(\lambda_i)}{\sqrt{T(\lambda_i)}}| > 3 \frac{\mathcal{L}(\lambda_i)}{\sqrt{2(N_{obs} - 1)}} \quad (3)$$

where we reject any spectral bin λ_i whose standard deviation along time departs from more than 3- SE_σ from the LOWESS fit \mathcal{L} , iterating until no more values are rejected with a maximum of 5 iterations.

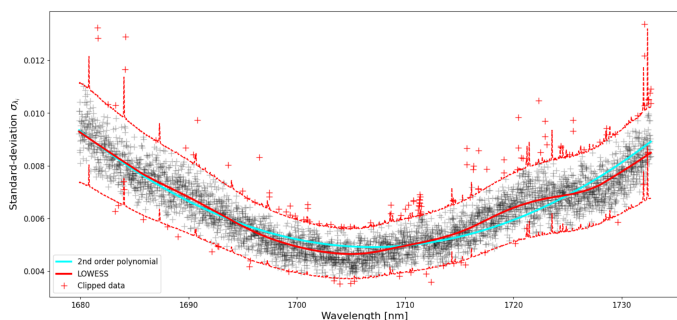


Fig. 5. Standard deviation computed for each spectral bin λ_i along the time axis as a function of the wavelength. A single SPIRou spectral order is shown here for illustration. The LOWESS fit (red) yield a better approximation of the error trend than the second-order polynomial fit (cyan), as for higher-degree polynomial fits (not shown). The upper and lower rejection thresholds are shown in red dashed lines, with the apparent peaks corresponding to telluric absorption lines. Data rejected after the first sigma clipping iteration are shown in red crosses.

6.2. Additional tables

Table 4. Linelists references for each species used in `petiTRADTRANS`.

Species	Reference
H ₂ O	HITEMP (Rothman et al. 2010)
CO	HITEMP (Rothman et al. 2010)
CH ₄	HITEMP (Hargreaves et al. 2020)
NH ₃	HITRAN (Rothman et al. 2013)
CO ₂	HITEMP (Rothman et al. 2010)
H ₂ S	HITRAN (Rothman et al. 2013)
HCN	Harris et al. (2006)
C ₂ H ₂	HITRAN (Rothman et al. 2013)
OH	HITRAN (Rothman et al. 2013)

Table 5. Prior distributions used in Nested Sampling Run 1 for all targets. All distributions are uniform within the specified range. The \log_{10} -MMR prior refer to the molecular abundances of all included species (H₂O, CO, CH₄, NH₃, CO₂, H₂S, HCN, C₂H₂, and OH).

Parameter	Prior (Run 1)
K_p [km s ⁻¹]	$\mathcal{U}(0, 500)$
V_0 [km s ⁻¹]	$\mathcal{U}(-20, 5)$
T_{iso} [10 ³ K]	$\mathcal{U}(0.2, 5)$
$\log_{10}(P_{cloud})$ [bar]	$\mathcal{U}(-6, 1)$
\log_{10} -MMR	$\mathcal{U}(-8, 0)$
V_{rot} [km s ⁻¹]	$\mathcal{U}(0, 15)$

6.3. Additional Corner Plots and CCF maps

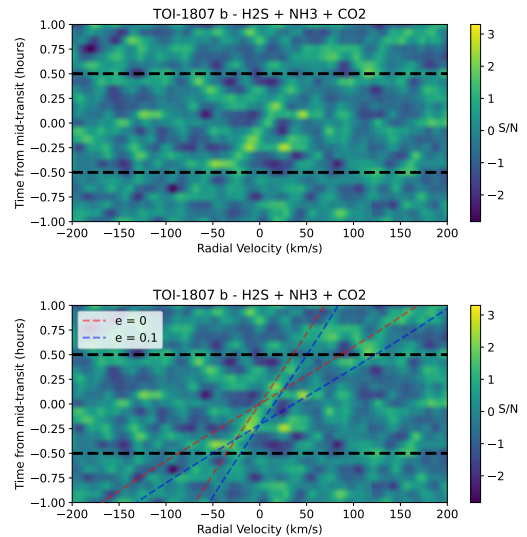


Fig. 6. Top: TOI-1807 phase-resolved CCF in the stellar rest frame as a function of planet's radial velocity and time from mid-transit. Horizontal black lines indicate start and end of transit; color indicates the S/N. **Bottom:** Same figure showing the planetary radial-velocity trail region permitted by uncertainties in M_p , K_s , and M_\star , for zero eccentricity (red) and $e = 0.1$ (blue).

¹¹ We used the implementation from the python module `statsmodels`

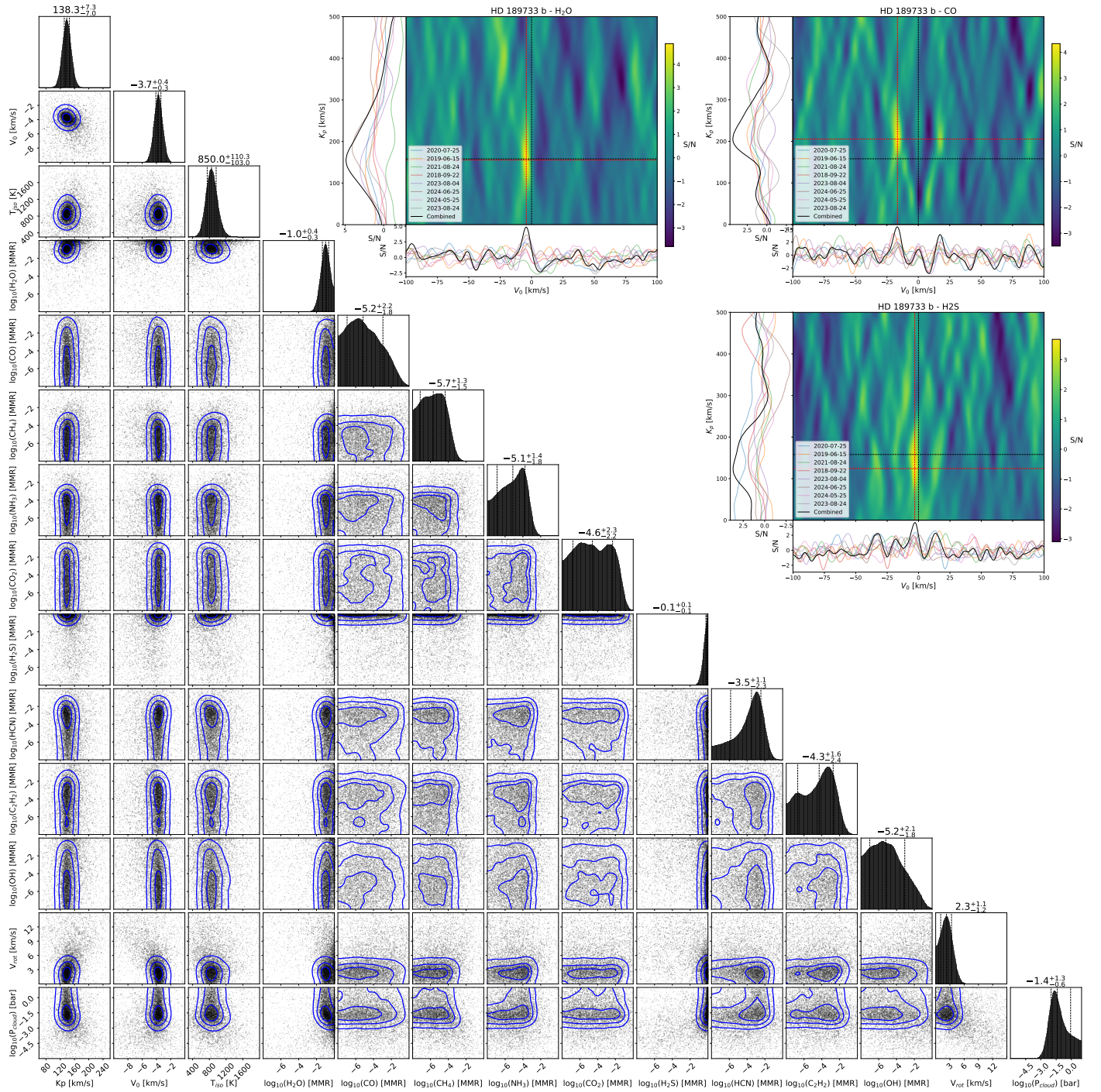


Fig. 7. Same as Fig. 2 for HD 189733 b.

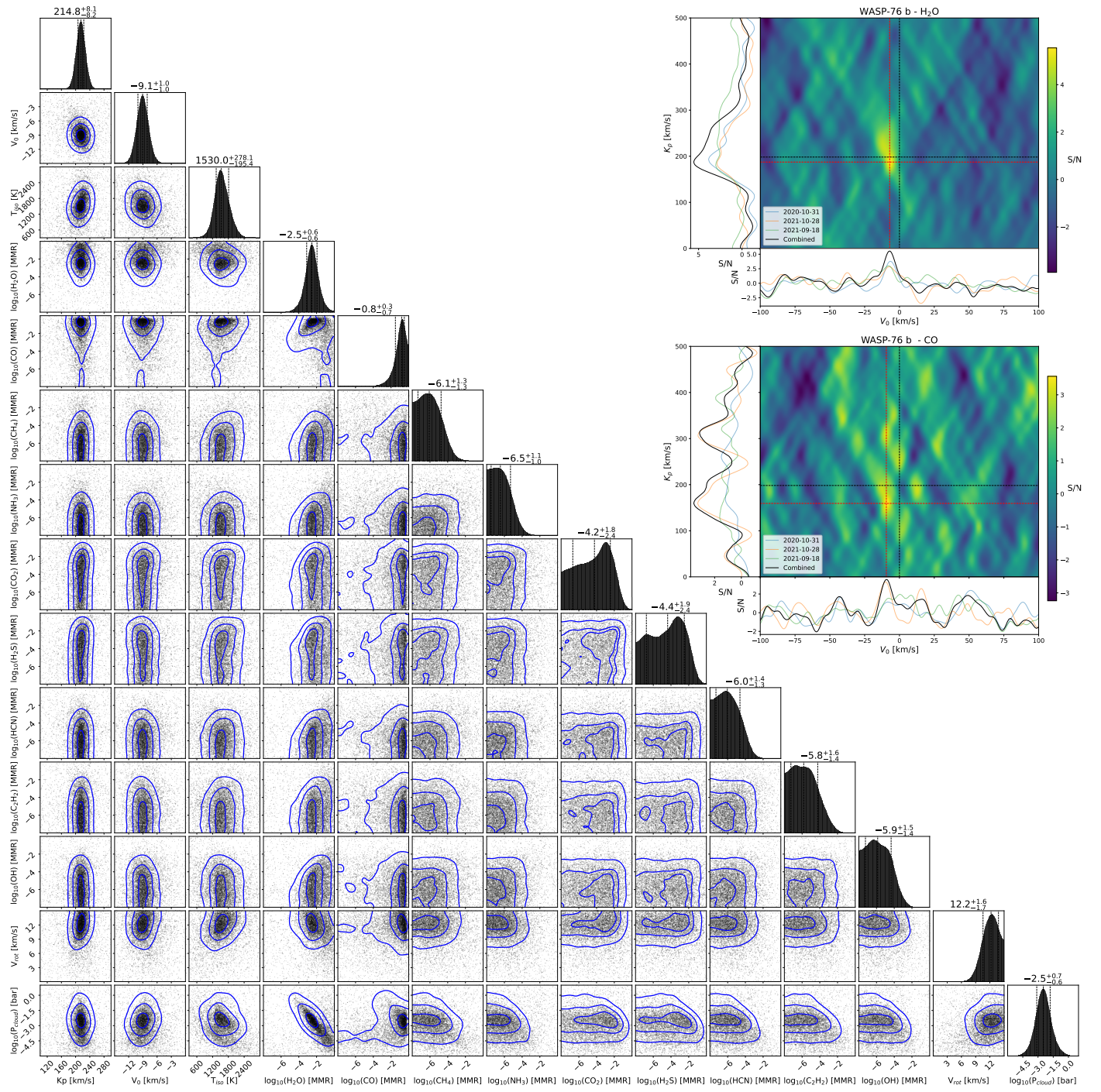


Fig. 8. Same as Fig. 2 for WASP-76 b.

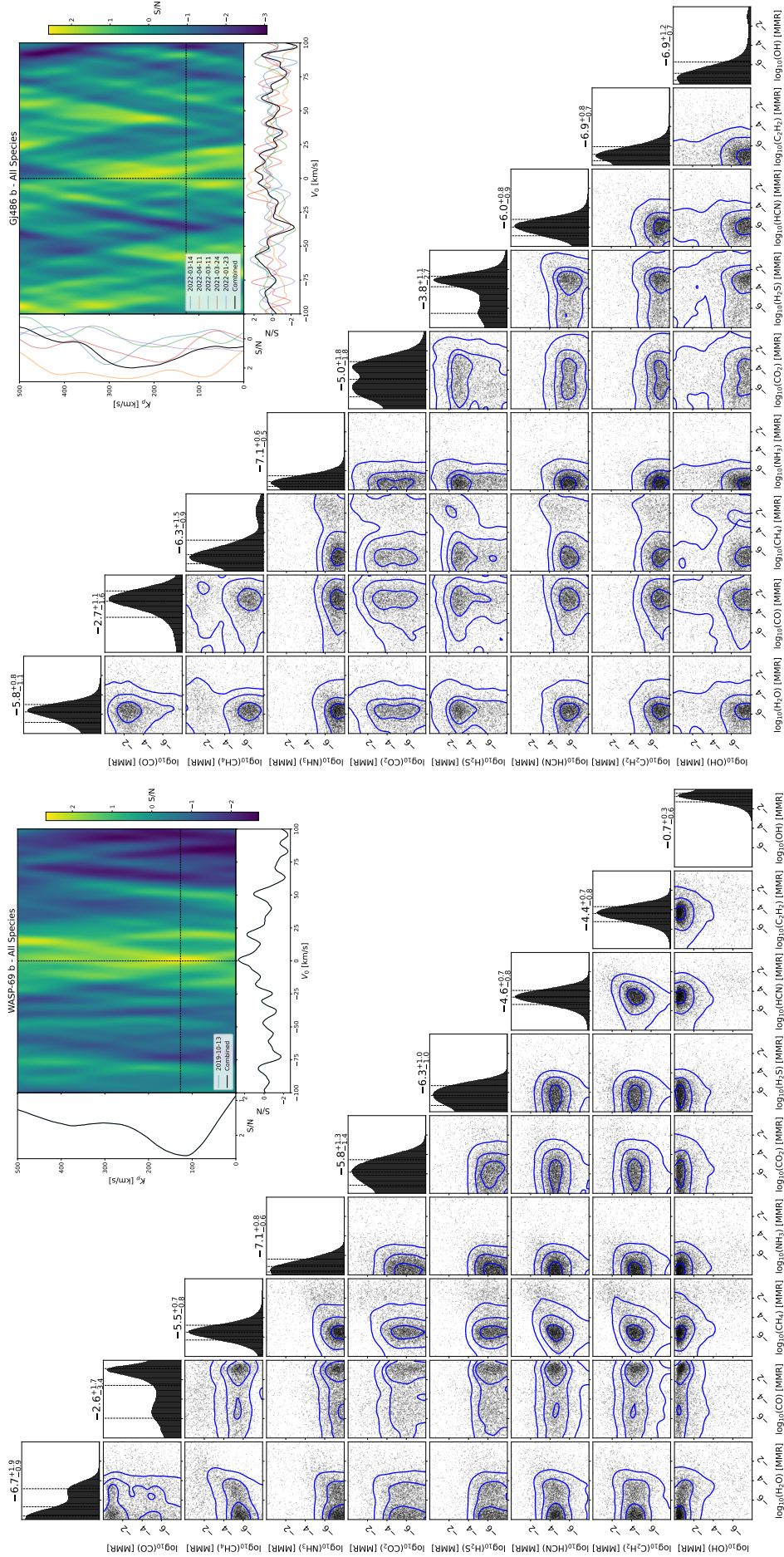


Fig. 10. Corner plot from the *Upper Limits Run* and associated CCF map for WASP-69 b (left) and GJ486 b (right). The blue contours represent the 1-, 2-, and 3- σ confidence intervals. The posterior distributions were obtained by fixing the isothermal profile to ExoREM's predictions and the mean molecular weight to 2.33 in a cloud-free model. The CCF maps were obtained with an atmospheric model including all species at their most favored abundances from the Run. The projected CCF at the planetary Kp and $V_0 = 0 \text{ km s}^{-1}$ (black cross) is shown in the left and lower CCF figure's panels for each transit date and for their combination (solid black). **Left:** although no convergence was found in the *Full run*, the posteriors from the *Upper Limit run* displayed here converged for CO, NH₃, HCN, C₂H₂, and at the upper edge of the prior for OH. The CCF map computed with all these species at their most favored abundance result in a 2.7- σ signal at the expected planetary position, though too weak to report a detection even tentative of the planet atmosphere. **Right:** the high CO abundance favored for GJ486 b may result from residual signatures of the M-dwarf host, and the CCF map obtained with all species at their best abundance shows no sign of a planetary signature.

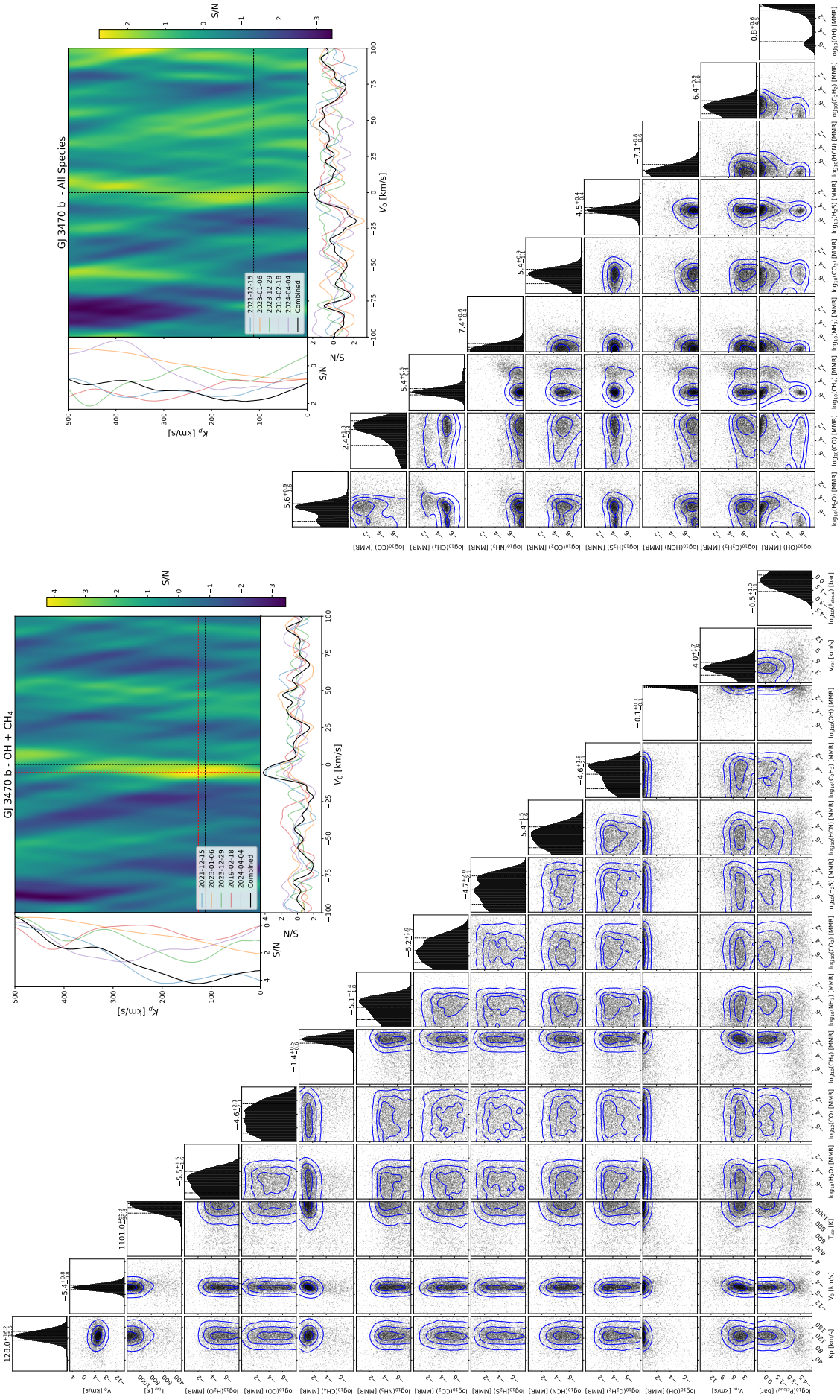


Fig. 11. Corner plot from the *Full* (left) and *Upper Limits* (right) Runs with associated CCF maps for GJ 3470 b. The blue contours represent the 1-, 2-, and 3- σ confidence intervals. **Left:** the posteriors converged toward a signature compatible with the planetary signal (black cross in the CCF), corresponding to a 4.3- σ tentative signature when computing a CCF map with an OH + CH₄ model with all parameters fixed to their best values. The projected CCF at the best Kp and V₀ km s⁻¹ found by the retrieval (red cross) is shown in the left and lower CCF figure's panels for each transit date and for their combination (solid black). **Right:** posteriors and CCF map obtained from the *Upper Limits Run*, i.e. by fixing the isothermal profile to ExoREM's predictions and the mean molecular weight to 2.33 in a cloud-free model. The CCF map was obtained using the best abundances and including all species, with the lower and left panels showing the CCF projected along the theoretical planet's position (black cross).

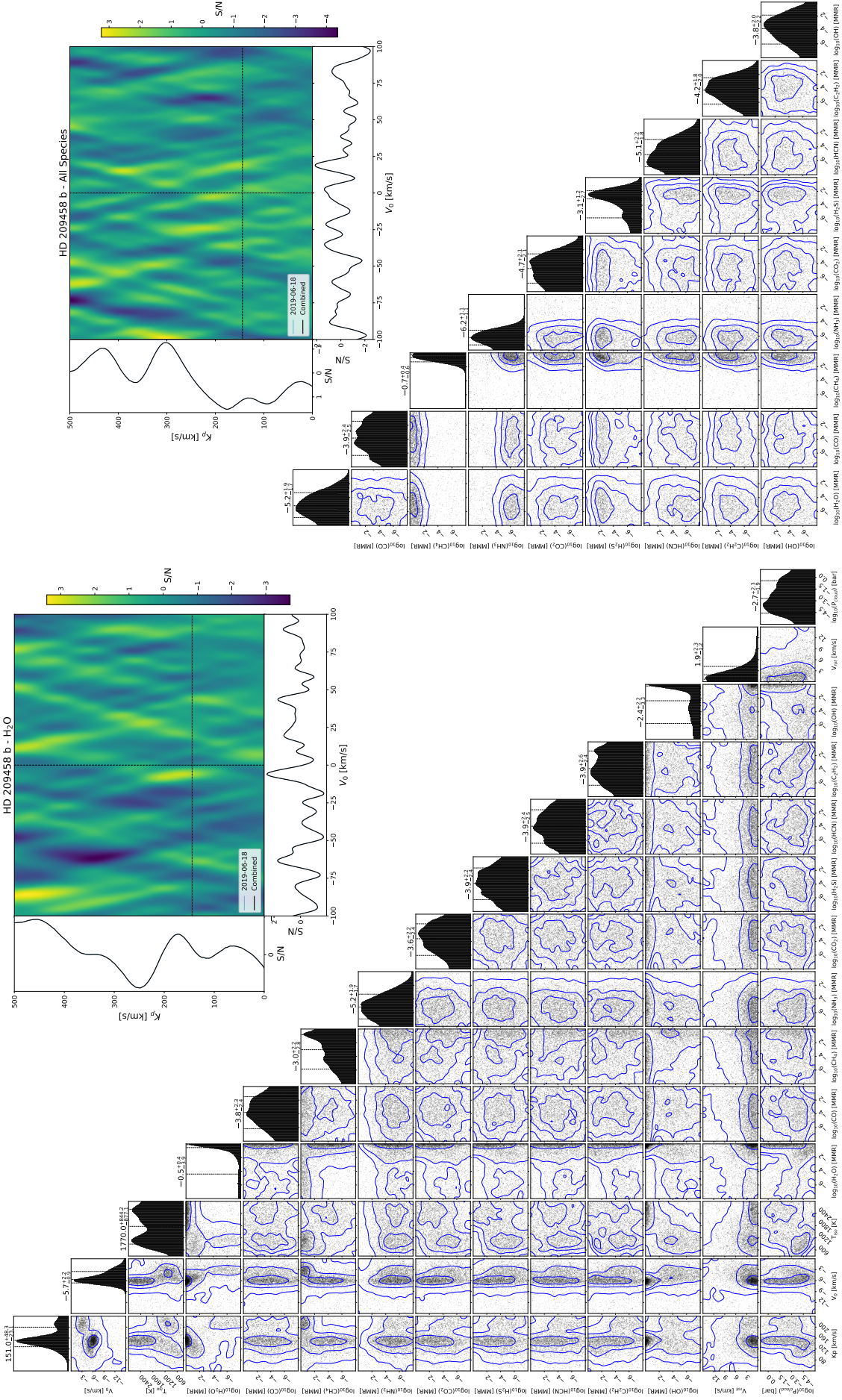


Fig. 12. Corner plot from the *Full* (left) and *Upper Limits* (right) Runs with associated CCF maps for HD 209458 b. The blue contours represent the 1-, 2-, and 3- σ confidence intervals. **Left:** the posteriors converged toward a signature compatible with the planetary signal (black cross in the CCF), yet corresponding to a 2.8- σ and therefore inconclusive signal in the CCF map computed from the best H₂O abundance found. The projected CCF at the best K_p and V₀ km s⁻¹ found by the retrieval (red cross) is shown in the left and lower CCF figure's panels for each transit date and for their combination (solid black). **Right:** posteriors and CCF map obtained from the *Upper Limits Run*, i.e. by fixing the isothermal profile to ExoREM's predictions and the mean molecular weight to 2.33 in a cloud-free model. The CCF map was obtained using the best abundances and including all species, with the lower and left panels showing the CCF projected along the theoretical planet's position (black cross).

